Chemical Geology 566 (2021) 120084

Contents lists available at ScienceDirect

Chemical Geology

journal homepage: www.elsevier.com/locate/chemgeo

Tectonic-controlled sediment-hosted fluorite-barite deposits of the central Alpine-Himalayan segment, Komsheche, NE Isfahan, Central Iran

Zahra Alaminia[a,*], Meisam Tadayon[a], Elizabeth Morris Griffith[b], Jesús Solé[c], Fernando Corfu[d]

[a] Department of Geology, Faculty of Science, University of Isfahan, P.O. Box: 8174673441, Isfahan, Iran
[b] The Ohio State University, School of Earth Sciences, 125 South Oval Mall, Columbus, OH 43210, USA
[c] Laboratorio Nacional de Geoquímica y Mineralogía and Instituto de Geología, Universidad Nacional Autónoma de México, Cd. Universitaria, Coyoacán, 04510 Mexico City, Mexico
[d] Department of Geosciences and CEED, University of Oslo, P.O. Box: 1047, Blindern, N-0316 Oslo, Norway

A R T I C L E I N F O

Editor: Michael E. Boettcher

Keywords:
Pb isotopes
Sr isotopes
Fluorite (U-Th)/He Thermochronology
Zefreh fault
Zagros orogeny

A B S T R A C T

The Triassic carbonate-hosted Komsheche deposit of Central Iran, in the central segment of the Alpine-Himalayan orogen, is an ideal test site for tectonic-controlled ore formation processes. The mineralization consists of barite, fluorite, minor galena, and subordinate pyrite and chalcopyrite, and gangue minerals of dolomite, quartz, siderite, organic material, and calcite. Radiogenic isotopes point to multiple sources. The Pb composition in galena indicates an origin of Pb from upper crustal material. Barite generations II and III have $^{87}Sr/^{86}Sr$ = 0.709147 to 0.709595, higher than those of the Triassic host rocks, but more similar to the composition of Paleozoic basement and Miocene seawater. The chondrite-normalized REE patterns of fluorite crystals are subhorizontal with slightly negative or no Eu anomalies and weak enrichment of the MREE. The composition of fluorite, combined with the Pb and Sr isotopic data, reflects a process of fluid-rock interaction for the mineralizing fluids along favorable lithological and structural sites. The anatomy of the Komsheche deposit is dominantly controlled by the fault architecture. The (U-Th)/He thermochronology of fluorite grains from Komsheche yields a range of ages from Early Cretaceous to Pliocene, in concordance with the multistage tectonic evolution of the Zagros orogen. Our proposed model is that the barite-fluorite deposits of Central Iran formed during alternating tectonic episodes, including Early Cretaceous extension, post-Cretaceous - Oligocene compression, Oligo-Miocene extension, and finally Miocene and younger compression. The spatial-temporal correlation of our results with those of other studies along the Alpine-Himalayan and Atlas Mountains domains reveal a tight coupling between tectonism and formation of sediment-hosted fluorine-bearing (±Ba, Pb±Zn) deposits throughout the Mesozoic and Cenozoic. Incipient deposits formed in the Mesozoic along extension-related basement faults and subsequent deposit generations formed during reactivation / inversion of pre-existing structures.

1. Introduction

In a wider perspective, the regional distribution of barite and fluorite deposits is closely linked to tectonic settings and fluid sources (Williams-Jones et al., 2000; Hein et al., 2007; Piqué et al., 2008; Magotra et al., 2017; Alaminia and Sharifi, 2018; Walter et al., 2018; Lepetit et al., 2019; Cansu and Öztürk, 2019; Öztürk et al., 2019; Jemmali et al., 2019; Hanilçi et al., 2019, 2020). Comparative studies of ore-forming fluid flow processes in sedimentary basins worldwide (e.g., Meyer et al., 2000; Kyser, 2007; Subías et al., 2010; Dill et al., 2012; Blasco et al., 2017; Jemmali et al., 2017; Cathles, 2019) reveal dynamic parameters and physico-chemical properties of fluids in geological time and space. This knowledge is essential for finding new exploration targets at deeper crustal levels (Kyser, 2007; Sośnicka and Lüders, 2019). Hence, the global spatial distribution of sediment-hosted fluorine-bearing (±Ba, Pb±Zn) deposits dominantly mimics the Atlantic rift margins and the Alpine-Himalayan orogenic belt. For instance, fluorite-barite vein deposits of Morocco, Tunisia, central and western Europe have been explained as the result of a large-scale regional mineralization event related to Pangea rifting (Fig. 1A; Galindo et al., 1994; Valenza et al., 2000; Staude et al., 2009; de Lamotte et al., 2009; Margoum et al., 2015; Kraemer et al., 2019; Walter et al., 2019; Lanari et al., 2020). Important

---

* Corresponding author.
E-mail address: z.alaminia@sci.ui.ac.ir (Z. Alaminia).

https://doi.org/10.1016/j.chemgeo.2021.120084
Received 23 June 2020; Received in revised form 8 November 2020; Accepted 22 January 2021

sediment-hosted fluorine-bearing (±Ba, Pb±Zn) deposits associated with Paleozoic to Paleogene carbonate units are found along the Alpine-Himalayan orogen (e.g., in Germany, Turkey, Iran, and China; see Fig. 1A and Table 1), the consequence of long-term subduction and collision processes following the Tethyan rifting (Berberian and King, 1981; Jolivet and Faccenna, 2000; Stampfli and Borel, 2002; Barrier et al., 2008; Hu and Stern, 2020). Other intrepretations for north Africa and Europe, Liu et al. (2015) suggest that the fluorite-rich carbonate-hosted Pb-Zn mineralization along the Himalayan-Zagros metallogenic province was closely related to the tectonic activities during the early Tertiary India-Eurasia collision.

In Iran, located in the middle segment of the Alpine-Himalayan orogenic belt, fluorite, with proven reserves of 1.7 Mt, is restricted to Permian to Early Cretaceous host rocks, while barite, with proven reserves of 5.3 Mt, is widespread in Late Precambrian to Pliocene host-rocks (Ghorbani, 2008, 2013). Most fluorite (±Ba, +Pb, ±Zn) deposits are located in the hinterland of the Zagros Orogen, usually adjacent to basement fault zones in central Iran (Fig. 1B). They are associated with the Malayer-Isfahan Pb-Zn metallogenic belt (Momenzadeh, 1976) at the northeastern border of the Sanandaj-Sirjan structural zone (SaS). They also occur in the Alborz belt, as well as in the Central East Iranian Microcontinent (CEIM). The latter are known as the Yazd-Anarak and Tabas-Poshtebadam metallogenic belts (Rajabi et al., 2013).

Fluorite+barite (hereafter FBA) deposits are stratabound in Early - Middle Triassic dolostones and to a lesser extent in Permian and Early Cretaceous carbonates (Table 1). Although the age of Triassic-hosted FBA deposits is still poorly constrained, they are assumed by some authors to be Early to Middle Triassic and syngenetic (Ghorbani and Momenzadeh, 1994; Ghorbani, 2013). FBA deposits are characterized by a simple mineralogy within a silicified and dolomitized wall rocks. They are sulfide-poor, usually associated with Pb, Zn, and minor Ag (Ghorbani, 2013; Rajabi et al., 2019). Due to their close association with the sediment-hosted Pb-Zn (±Ba) deposits, FBA deposits have originally been interpreted as Mississippi Valley-Type systems, classified as F-rich MVT deposits (e.g., Alirezaei, 1985; Gorjizad, 1995; Rostami, 2001; Rajabzadeh, 2007; Shamsipour Dehkordi et al., 2011; Rajabi et al., 2013; Karimpour and Sadeghi, 2018). By contrast, some authors proposed a syn-sedimentary to early diagenetic origin for some sediment-hosted Zn-Pb (±Ba ±Ag) deposits (Momenzadeh, 1976; Rastad, 1981; Ghorbani, 2013; Boveiri Konari et al., 2016; Boveiri Konari and Rastad, 2017; Niroomand et al., 2019). Rajabi et al. (2013) suggest that fluorite-rich deposits could be linked to normal faults developed in the Late

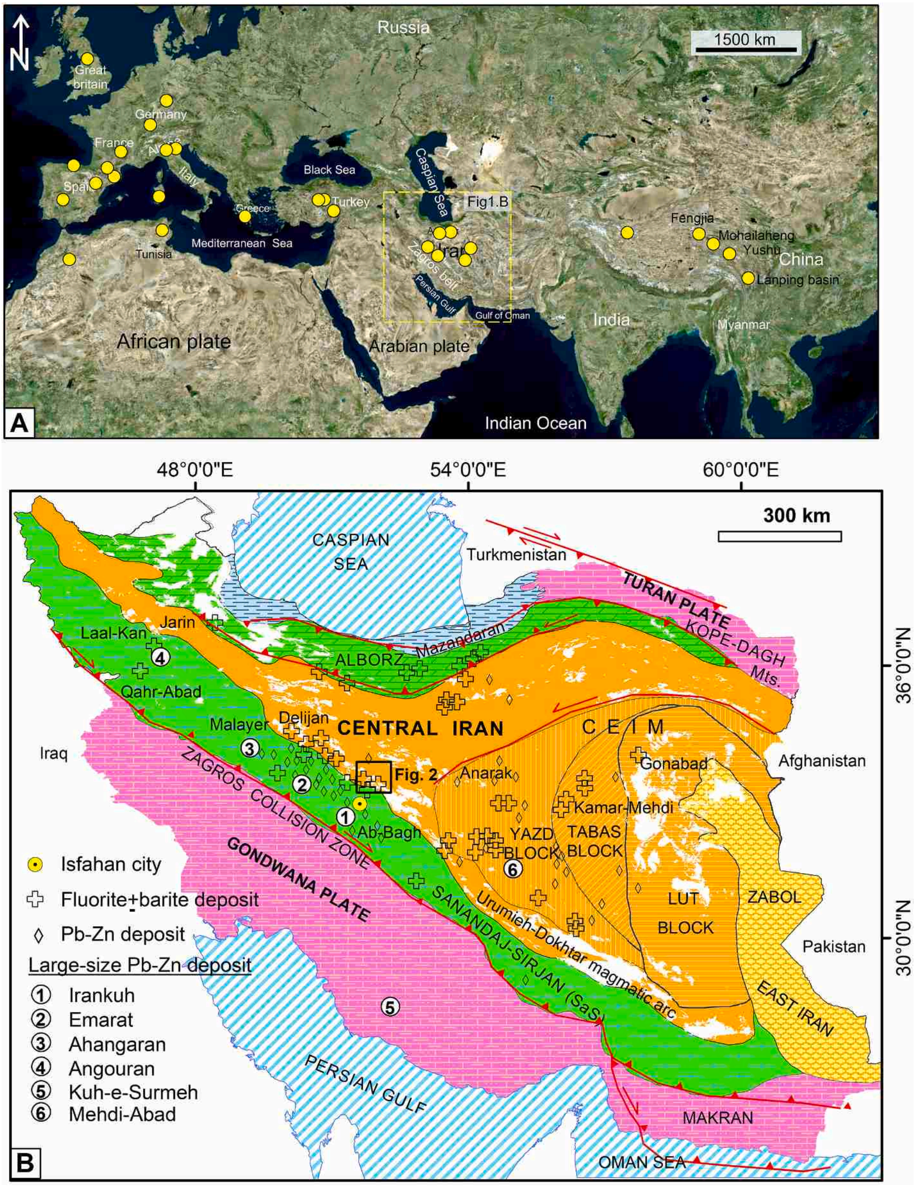

Fig. 1. (A) Satellite image of the Alpine–HimalayanTethyan orogenic belt, showing spatial distribution of sediment-hosted fluorite-rich (±Ba, Pb±Zn) deposits. Please see Table 1. Yellow dashed rectangle shows location of Fig. 1B. (B) Map of Iran showing major tectonic zones and distribution of carbonate-hosted deposits of fluorine, barium, lead and zinc (modified after Aghanabati, 1998; Rajabi et al., 2013). Black square indicates the location of Fig. 2 and Komsheche deposit. White patches on the structural zones (mostly Central Iran) showing Cenozoic magmatism of Iran. CEIM: Central East Iranian Microcontinent, SaS: Sanandaj-Sirjan.

Table 1
Comparison of the characteristics of FBA deposits of Iran with sedimentary rock-hosted fluorite (±Ba, Pb±Zn) deposits of Asia, Europe, and north Africa.

Name of deposit	Age of host rock	Mineralogy	Wall rock alteration	Temperature and salinity	δ^{34}S (permil)	Ore type, process, setting	Sources
Central Iran							
Komsheche	Middle Triassic dolomite	Brt, Fl, Gn, Cal, Qz	silicification, dolomitization	Th_{Fl}=89-244°C Th_{Brt}=119-323°C 10-12 wt.% NaCl	(23-27) Brt	MVT	Rajabzadeh (2007)
Pinavand	Early Cretaceous	Fl, Brt, Gn, Cal, Qz	silicification, dolomitization	Th_{Fl}=85-235°C 9-36 wt%NaCl	(5-17) Brt	diagenesis	Qishlaqi and Moore (2006); Shafaezadeh (2012)
Kamar-Mehdi	Middle Triassic dolomite	Fl, Brt, Gn, Cal, Dol	dolomitization	Th_{Fl}=150-270°C 15-26 wt% NaCl		diagenesis MVT	Pirouzi et al. (2009)
Ardakan Yazd	Late Devonian, Early Carboniferous, Permian	Fl, Gn, Brt, Cpy, Qz, Py	silicification	Th_{Fl}=150-182°C 2-7 wt%NaCl		associated with magmatic activity (204 Ma)?	Rahimpour-Bonab and Shekarifard (2002)
Ravar, Kerman (Kuhebanan)	Triassic dolomite	Brt, Fl, Gn, Sp	silicification				Ghorbani (2008)
Tazareh (Shahrood)	Early Triassic dolomite	Brt, Fl, Gn, Sp	silicification				Ghorbani (2013)
Sefid-Kouh	Jurassic limy mudstone	Fl, Qz, Brt, Cal	silicification	Th_{Fl}=125-181°C 2-8 wt.%NaCl			Pazhkhzade et al. (2018)
Delijan (Atash-Kuh, Bagherabad, Dare-Badam)	metamorphosed Early Jurassic- Mid. Cretaceous dolomite	Brt, Fl, Gn, Dol, Cal, Cpy, Py, Chl	dolomitization, silicification,	Th_{Fl}=90-205°C 18-23 wt.% Th_{Brt}=130-270°C 4-10 wt.%NaCl			Moghaddasi et al. (2016)
Bozijan	Early Jurassic Shemshak Fm.	Fl, Qz, Cal, Gn, Py, Mn oxide	argillization, silicification	Th=152-390°C 15-25 wt.% NaCl		unconformity-related fluorite deposit	Ehya (2011)
Alborz							
E Mazandaran (Savad-kuh, Kiasar, Pachi-miana, Kamar posht, Abgarm, Era, shashroodbar)	Middle Triassic dolomite	Fl, Brt, Gn, Cal, Py, Dol (epigenetic and syngenetic)	silicification, dolomitization	Th=200-250°C	(-2)-(12) Gn (13-26) Py (23-48) Brt	MVT, Ore diagenetic and post diagenetic; formed during Cimmerian event	Zabihitabar et al. (2017); Vahab-zadeh et al. (2008); Nabiloo et al. (2017); Alirezaei (1985); Mehraban (2016)
Oras-Kuh	Triassic Elika Fm.	Gn, Sph, Py, Dol, Cal, Brt, Qz, Fl	dolomitization	Th_{Brt}=298-323°C 0.6-15 wt.% NaCl		MVT, Alpine orogeny	Lotfi et al. (2015)
Jarin, Zanjan	Cretaceous carbonate	Brt, Fl, Gn, Cal, Py, Dol	dolomitization, silicification, argillization	Th_{Fl}=145-165°C 13-15 wt.% NaCl Th=130-259°C 0.8-8 wt.% NaCl		MVT	Kouhestani and Mokhtari (2017)
Sanandaj-Sirjan							
Farsesh	Permian carbonate	Brt, Cal, Dol, Qz, Cpy, Py	silicification, dolomitization	Th=125-200°C 4-20 wt.%NaCl		seawater-bearing hydrothermal fluids	Zarasvandi et al. (2014)
Qahr-Abad	Permo-Triassic dolomite	Fl, Cal, Dol, Qz	argillization, silicification			hydrothermal	Talaie and Abedini (2012); Alipour et al. (2015)
Laal-Kan	Paleozoic schist	Cal, Fl, Qz, Brt, Hm		Th=118-151°C 19-23wt.% NaCl		hydrothermal, (< 95 Ma)	Rezaei-Azizi et al. (2018)
Turkey							
Göktepe province (Tauride)	Permo-Triassic limestone	Gn, Sp, Fl, Cal, Brt, Py	silicification, dolomitization	Th=58-154°C 14-21 wt.% NaCl		MVT Diagenesis	Hanilçi et al. (2019)
Feke (Adana)	carbonate					MVT	Uras et al. (2003)
Pöhrenk (Anatolia)	Eocene-Miocene sediments	Fl, Qz, Cal, Dol, Brt	dolomitization			Miocene-Pliocene	
		Fl, Brt, Gn					Genç (2006)
Greece	Marble, schist, metavolcanic	Ag-Gn, Qz, Cal, Fl, Sph		Th=92-207°C 17wt.%NaCl		internal zone of the Miocene orogen, hydrothermal	Scheffer et al. (2019)
Italy N Italy	Triassic, Permian	Gn, Sph, Fl, Brt				MVT	Omenetto (1979)
Palermo (NW Sicily)						hydrothermal	Bellanca et al. (1987)

(continued on next page)

Table 1 (*continued*)

Name of deposit	Age of host rock	Mineralogy	Wall rock alteration	Temperature and salinity	$\delta^{34}S$ (permil)	Ore type, process, setting	Sources
	Jurassic, Cretaceous limestone	Fl, Brt, Qz, Cal, Dck	silicification, dolomitization	Th_{Fl}=60-300°C Low salinity			
SE Sardinia	Paleozoic	Fl, Gn, Brt, Sph, Cal		Th=120-180°C 0-18 wt.%NaCl		Post Variscan orogen	Mondillo et al. (2017)
Germany SW Germany (Schwarzwald)	Early Triassic redbed, Jurassic, Late Cretaceous to Paleogene	Brt, Fl, Qz, Sph, Gn, Cal		*Th_{Gr3}=50-150°C 0-20wt.%NaCl *Th_{Gr4}=50-150°C 13-18wt.% NaCl	(12-45) Brt_{Gr3} (13) Brt_{Gr4}	Paleogene barite, secondary Miocene barite, Alpine orogen	Staude et al. (2011)
N Germany (Harz Mts.)	Ordovician to Carboniferous, Permian siliciclastic sediments	sulfide, Brt, Fl, Qz		Th=100-120°C high salinity		Variscan orogeny (226-209 Ma), Late Cretaceous	Nadoll et al. (2018); Graaf et al. (2019)
Spain NE Spain, Berta in Catalonian Coastal Range	Carboniferous, Triassic (evaporite and carbonate)	Fl, Qz, Brt, Cal, Gn, Cpy, Py		Th=100°C 21 wt.%NaCl	(15-20) Brt	Miocene; other deposits formed between 225 and 195 Ma	Canals and Cardellach (1993); Galindo et al. (1994)
Asturias	Permo-Triassic and Paleozoic	Fl, Qz, Brt, Cal, Dol, Sph, Py, Gn, Cpy	silicification, chloritization	Th=80-170°C 7-14 wt.%NaCl	(17-31) Brt	185 Ma, pre-rift or contemporaneous to Atlantic ocean opening	Sánchez et al. (2010)
Iberian	Triassic arenites, Ordovician-Devonian limestones	Brt, Sph, Gn, Fl, Py, Cpy, Qz, Sd	dolomitization	Th=180°C 4 wt.%NaCl Th=120-130°C 20 wt.%NaCl	(15-28) Brt	Mesozoic extensional events	Subías et al. (2010)
Parzan, Caravia-Berbes	Late Paleozoic, Triassic	Gn, Py, Cpy, Sph, Fl, Brt, Qz, Sd, Dol	silicification, chloritization, sericitization	Th=117-195°C 10-24 wt.% NaCl		Aptian-Albian, 115±3 Ma	Fanlo et al. (1998); Symons et al. (2017)
China Sanjiang belt, Tuotuohe	Carboniferous to Triassic	Gn, Sph, Fl, Brt, Cal, Dol, Py	dolomitization	Th=70-370°C 6-28 wt.%NaCl	(-30)-(7.4) sulfide	Fl-bearing sub-type of MVT (32-38 Ma), Chaqupacha (<16 Ma), Jinding (~65 Ma)	Tian et al. (2009); Song et al. (2015); Liu et al. (2017)
Fengjia, Longxi	Early Ordovician carbonate	Fl, Brt, Cal, Qz, Py, Ser	calcitization, silicification, sericitization, kaolinization	Th=86-302°C 0.2-21 wt.% NaCl		intra-continental Himalayan orogeny, formed by meteoric and metamorphic fluids, 104-129 Ma	Zou et al. (2015, 2017)
Mohailaheng	Carboniferous, Permian to Triassic	Sph, Gn, Py, Cal, Fl, Brt, Qz, Dol	dolomitization	Th=130-180°C 19-24 wt.% NaCl		Early Tertiary Himalayan orogeny	Liu et al. (2015)
Great Britain, UK (Pennine orefield)	Carboniferous marine strata	Gn, Sph, Fl, Brt		Th=99-160°C ~20 wt.%NaCl	~basinal brine	Fl-bearing sub-type of MVT (~175 Ma), opening of the Atlantic	Kraemer et al. (2019)
France (S Massif Central)	Paleozoic	Fl, Cpy, Apy, Qz, Sd		Th=120-210°C 20-26 wt.% NaCl		MVT (~111Ma)	Munoz et al. (2005)
Tunisia NE Tunisia (Zaghouan)	Jurassic, Cretaceous, Miocene	Fl, Brt, Gn, Sph		Th=100-250°C 12-34 wt.% NaCl	(15-22) Brt	Post Jurassic to Late Miocene, related to fault reactivation during Late Miocene	Souissi et al. (1997); Souissi et al. (2013) Jemmali et al. (2019)
					(14.8-15.4) Brt		
Morocco	Permo-Triassic to Cretaceous red beds	Fl, Brt, Qz		Th=94-174°C 14-24 wt.% NaCl	(9-15) Brt	Related to central Atlantic rifting (~220 and 155 Ma)	Valenza et al. (2000); Margoum et al. (2015)

Abbreviations of Whitney and Evans (2010): Apy-arsenopyrite, Brt-barite, Cal-calcite, Chl-chlorite, Cpy-chalcopyrite, Dck-dickite, Dol-dolomite, Fl-fluorite, Gn-galena, Hem-hematite, Py-pyrite, Qz-quartz, Sd-siderite, Ser-sericite. MVT: Mississippi Valley-type.

* Schwarzwald data is of barite groups- 3 and -4.

Triassic foreland basin during the closure of the Paleo-Tethys in the Cimmerian orogeny. Recent geochemical results of FBA deposits in the Central Alborz metallogenic belt (Fig. 1B) reveal that fluorite was deposited epigenetically during at least two stages of diagenesis (Zabihitabar and Shafiei-Bafti, 2015; Moghaddasi et al., 2016; Nabiloo et al., 2017; Kouhestani and Mokhtari, 2017; Zabihitabar et al., 2017).

Central Iran represents the wide hinterland of the Zagros orogen. It is covered by thick Paleozoic - Mesozoic carbonate successions, which host extensive FBA deposits next to NW-SE to N-S-trending intraplate fault zones. Typical occurrences are the Pinavand, Kamar-Mehdi, and Mehdi-Abad deposits (Fig. 1B). The Isfahan province, located in the Malayer-Isfahan metallogenic belt, is broadly the host of several similar FBA occurrences, including the world-class Irankuh Pb-Zn deposit (Esmaeili Sevieri et al., 2019) and numerous smaller Pb-Zn deposits (Fig. 1B). FBA clusters are hosted in Triassic and Early Cretaceous carbonate rocks (Fig. 2), while Pb-Zn deposits occur mostly within Cretaceous carbonates.

The Triassic-hosted Komsheche deposit, 100% owned and discovered in 1968 (Burnol, 1968), is located 76 km northeast of Isfahan and is one of the best-known barite and fluorite producing occurrences. Former

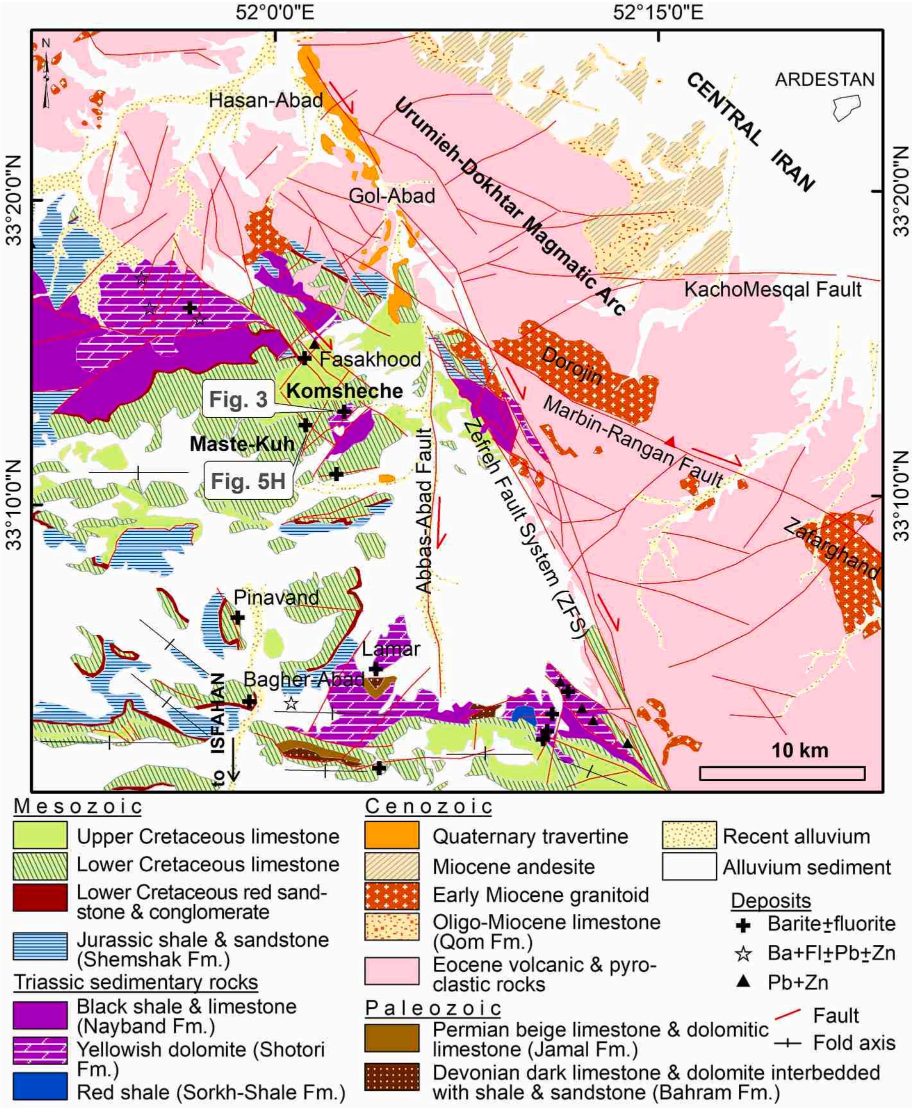

Fig. 2. Simplified geological map of northeast Isfahan (modified after Radfar et al., 1999; Mannani and Yazdi, 2009; Habibi et al., 2013) showing the Triassic-hosted Komsheche, Cretaceous-hosted Pinavand, and all FBA deposits hosted in carbonate rocks.

studies of the Komsheche deposit show that fluorite precipitated at temperatures between 89° and 244°C with a mode at 150°C, from aqueous solutions containing traces of hydrocarbons with variable salinities (0 - 25.4 wt % NaCl equiv). Micro-thermometric results from fluid inclusions in the barite yield relatively high temperatures (between 119° and 323°C, with two modes at 150° and 250°C) and salinities from 0 to 20.6 wt % NaCl equiv that are consistent with a hydrothermal environment associated with Na, Ca, and Mg ionic species in the fluid (Rajabzadeh, 2007). By contrast, based on geochemical arguments, the Cretaceous-hosted Pinavand fluorite (about 17 km southwest of Komsheche in Fig. 2) is interpreted to have formed in a sedimentary system (Qishlaqi and Moore, 2006; Shafaezadeh, 2012). Only a few studies have been done on barite deposits in contrast to numerous investigations on Pb-Zn deposits (e.g., Ehya et al., 2010; Rajabi et al., 2012, 2013). For instance, Ghazban et al. (1994) suggested that barite in the Cretaceous carbonate-hosted Irankuh Pb-Zn±Ba deposit was not derived from normal seawater, based on the high $^{87}Sr/^{86}Sr$ ratios of barite and carbonate. These characteristics are likely due to the incorporation of Sr from marine carbonate, whereas the lead isotopic data point to an oceanic slab source contaminated with lead from the continental crust (Karimpour and Sadeghi, 2018; Esmaeili Sevieri et al., 2019). A recent pyrite Re-Os isochron age of 66.5±1.6 Ma from Irankuh supports a Late Cretaceous age for the mineralization (Liu et al., 2019). In the Ab-Bagh Zn-Pb±Ba deposit, Paleozoic sedimentary basement is believed to be the most probable origin for the metal-rich fluids, as suggested by the more radigenic Sr isotope values of hydrothermal calcite (Movahednia et al., 2020).

Several studies (Rajabzadeh, 2007; Ghorbani, 2013) have shown that the age relationships between FBA and host rocks are not well understood and both syngenetic and epigenetic origins have been debated. To address this gap, we have applied a multidisciplinary approach with fluorite (U-Th)/He geochronology, Pb and Sr isotope analyses, and structural analysis to one of the outstanding FBA deposits in Central Iran. Our paleohydrological reconstructions and deciphering of the ore-forming processes shed light on the long-term tight linkage between FBA mineralization and the tectonic evolution in the overriding plate of the Zagros orogen through Mesozoic to Pliocene time.

2. Geological evolution of Central Iran

The CEIM and SaS were detached from the northern margin of Gondwana during the initiation of the Neo-Tethys Ocean in the Early Permian and collided with the southern margin of Eurasia (Turan Plate) in the Late Triassic, thereby closing the Palaeo-Tethys (Eo-Cimmerian event; e.g., Stöcklin, 1974; Stampfli and Borel, 2002; Fürsich et al., 2009; Wilmsen et al., 2009). Northward subduction of the Neo-Tethys beneath the southern margin of the Iranian plate initiated in the Late Triassic (Arvin et al., 2007; Hassanzadeh and Wernicke, 2016; Sheikholeslami, 2016) and subsequently produced a magmatic arc (Berberian and Berberian, 1981; Hassanzadeh and Wernicke, 2016). This process is thought to have reduced compressive stress on the internal parts of the Iranian plate, leading to the formation of extensional basins, which subsequently were filled by thick piles of Late Triassic marine sediments (Nayband Fm. of Central Iran; Fürsich et al., 2005a). The main Cimmerian event resulted in the termination of marine sedimentation, followed by non-marine deposition or erosion of source-areas on the Iranian plate during the Jurassic (Wilmsen et al., 2009; Salehi et al., 2018). This event may have been initiated by break-off of the subducting slab of the Palaeo-Tethyan Ocean beneath the Turan Plate around the Triassic–Jurassic boundary (Fürsich et al., 2005b, 2009; Wilmsen et al., 2009). Thousands of meters of Jurassic sediments, such as the Shemshak Fm., were uncomfortably deposited on the west of the CEIM (Wilmsen et al., 2010; Senowbari-daryan et al., 2010; Ghasemi-Nejad et al., 2013; Fürsich et al., 2016). The Late Cimmerian event (Late Jurassic–Earliest Cretaceous) was marked by block faulting, sedimentation of conglomerates and red beds, and stratigraphic gaps in many places on the Iranian plate (e.g., Wilmsen et al., 2010, 2013, 2015), and counter-clockwise block rotation in the CEIM (Mattei et al., 2015). On top of the Shemshak Fm. strata, there is a Late Cimmerian unconformity overlain directly by Early Cretaceous red beds (Zahedi, 1976; Radfar et al., 1999; Aghanabati, 2004). Shemshak Fm. and Early Cretaceous red beds mark a sharp transition from a high-energy continental Late Triassic - earliest Cretaceous deposition of detrital strata to sedimentation of thick marine Early to Late Cretaceous carbonates on the stable platform and development of oceanic back-arc basins in-between the CEIM fragments (Barrier et al., 2008; Tadayon, 2013; Wilmsen et al., 2015; Shafaii Moghadam and Stern, 2015: Salehi et al., 2018). Late Cretaceous–Early Paleocene time corresponds to the onset of northeast-ward subduction of the Neo-Tethyan oceanic plate beneath the CEIM (Stöcklin, 1968; Berberian and King, 1981; Jolivet and Faccenna, 2000; Hassanzadeh and Wernicke, 2016). It resulted in obduction of ophiolites along the Zagros suture zone and oceanic back-arc basins (Agard et al., 2005, 2011; Shafaii Moghadam et al., 2009; Mouthereau et al., 2012), as well as reactivation of Cretaceous normal basin boundary faults as high angle reverse faults in the central SaS (Salehi and Tadayon, 2020). In the Late Eocene–Oligocene continental collision occurred and the Urumieh-Dokhtar Magmatic Arc (UDMA) was formed (Berberian and Berberian, 1981; Berberian and King, 1981; Jolivet and Faccenna, 2000; Mouthereau et al., 2012; Chiu et al., 2013). A major tectonic reorganization followed in the Middle–Late Neogene along the Zagros convergence zone, initiating the recent NW-SE right-lateral transpressional main Zagros fault (Jackson, 1992; Talebian and Jackson, 2002; Mouthereau et al., 2012) and reactivating CEIM basement faults (Allen et al., 2004; Austermann and Iaffaldano, 2013; Tadayon et al., 2017).

The westernmost Central Iran domain developed an elongate NW-SE trending basin between the SaS in the southwest and UDMA in the northeast (Fig. 1B). The Komsheche study area is located in the western part of the Central Iran domain (Fig. 1B), adjacent to main basement faults, such as the Zefreh Fault System, hereafter ZFS, and Abbas-Abad Fault (Fig. 2), and in a geological province with a protracted tectonic evolution history.

2.1. *General geology of FBA mineralized area*

In northeast Isfahan, numerous FBA mineralized areas (e.g., Komsheche, Pinavand, and Fasakhood) crop out in the Mesozoic basement on the western shoulder of the ZFS (Fig. 2). The lithostratigraphy of the FBA mineralized area is characterized at the base by a series of dark grey dolomite and conodont-bearing limestone interbedded with two beds of phosphate, sandstone, and sandy limestone dated as Devonian (Bahram Fm.) (Bahrami et al., 2015). Bahram Fm. is disconformably overlain by relatively thick Late Permian *Gymnocodium*-bearing gray limestone, dolomitic limestone, dolomite, and sandstone (Jamal Fm.) (Radfar et al., 1999; Ameri et al., 2017). This unit is unconformably followed by Early to Middle Triassic strata consisting of 10 m of ferruginous dark quartzite with few meters of red shales (Sorkh-Shale Fm.) at the base, Middle Triassic thick yellowish dolostone (Shotori Fm.), gray conglomerate with reddish sandstone intercalations, shale and dark shale with quartz sandstone and dolomitic limestone intercalations and *Heterastridum*-bearing limestone on top (Nayband Fm.) (Radfar et al., 1999; Aghanabati, 2004). These strata are unconformably capped by dark gray coaly shale and sandstone with intercalation of thin limestone (Shemshak Fm.) that is attributed to the Late Triassic-Middle Jurassic Eo-Cimmerian event (Radfar et al., 1999; Salehi et al., 2018).

The Cimmerian package is unconformably covered by thick Early Cretaceous red beds that consist of brown conglomerate with voids filled by evaporites at the bottom and fining upward red sandstone on top (Salehi et al., 2018). It is followed by a continuous thick pile of Early to Late Cretaceous *Orbitolina*, rudist, ammonite and *Inoceramus*-bearing limestones intercaled by olive shale (Radfar et al., 1999; Aghanabati, 2004). The Paleogene in the northeast of Isfahan emerged with gray conglomerate overlain by an about 2 km thick sequence of various types of volcanic rocks and rare intercalations of nummulitic sandy limestone and shale (Radfar et al., 1999; Alaminia et al., 2017). This Paleogene package is unconformably covered by cream limestone and marl at the bottom and an alternation of limestone and andesitic lava on top (Qom Fm.) (Radfar et al., 1999; Aghanabati, 2004). Early Miocene intrusives include the Dorojin and Zafarghand granitoids (Sarjoughian et al., 2017; Alaminia et al., 2020). The development terminated with latest Miocene-Pliocene conglomerate and sandstone (Radfar et al., 1999). Eventually, Quaternary hot spring-related travertine formed along the active fault zones and alluvial sediments covered everything (Fig. 2; Radfar et al., 1999; Beygi et al., 2016).

3. Komsheche deposit

The FBA is located approximately 1.5 km shouthwest of Komsheche village, southwest of Ardestan (Fig. 2). The strata exposed around the mine are Triassic sediments, unconformably overlain by Early Cretaceous strata (Fig. 3A). The Triassic sedimentary succession is subdivided into three formations (Fig. 3A): 1) the Early Triassic Sorkh-Shale Fm, with intercalating red sandstone and carbonate; 2) the Middle Triassic Shotori Fm. consisting of yellowish dolomite; and 3) the Late Triassic Nayband Fm. characterised by dark shale and dark green sandstone beds with intercalations of fossiliferous limestone. At the Komsheche mine the Shotori Fm. and Nayband Fm. were folded. Jurassic strata are missing in the Komsheche mine area. This is attributed to the Cimmerian orogeny-related uplift (Radfar et al., 1999; Mannani and Yazdi, 2009; Nützel et al., 2010) (Fig. 3A). The Late Triassic sequence is covered by a transgressive unit of red conglomerate, up to 2 m thick, at the base of the Early Cretaceous. The basal bed of conglomerate comprises pebbles of Shotori dolomite and siliciclastic rocks and some thin coal beds without any sign of Jurassic fossils (Mannani and Yazdi, 2009). The red conglomerate is capped by calcareous sandstone, dolomite, grey *Orbitolina*-bearing limestone, sandy limestone, marl, and shale (Radfar et al., 1999).

The FBA mineralization in the Komsheche deposit is found dominantly along the faulted contacts that are mainly concentrated in yellowish dolostone of the Middle Triassic Shotori Fm, but it also occurs in the Late Triassic Nayband Fm. (Figs. 3A and 5F) and in Early Cretaceous limestone (Fig. 5H). The ore bands are sub-parallel to the fold-axis of a syncline with a Triassic core that was uplifted by later tectonic events. Large pebbles of ore-bearing Cretaceous limestone in faulted Nayband Fm., geological field observations, and cross-cutting relationships suggest a post-Cretaceous age for the FBA mineralization. However, the banded (stratabound) FBA mineralization in rudist-bearing

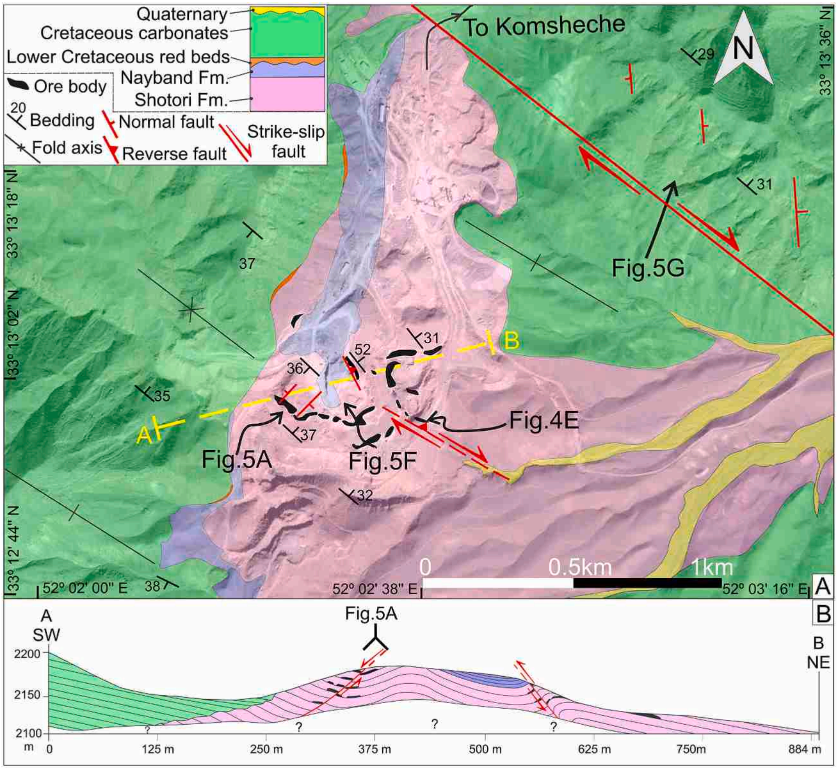

Fig. 3. (A) Geological map and synthetic stratigraphic column of the Komsheche deposit with distribution of ore body, northeast of Isfahan (modified and readapted after Radfar et al., 1999). For location see Fig. 2. (B) NE–SW-oriented interpretative geological cross-section across the study area.

Early Cretaceous carbonates, about 1 km north of the Komsheche mine and its surrounding FBA mines (e.g., Fasakhood and Maste-Kuh mines) (Fig. 2), could indicate at least an Early Cretaceous age for FBA mineralization. Noteworthy, field observations in the mining area show that the Komsheche deposit was not associated with magmatic or volcanic activity.

The Komsheche mine consists of about 20 discontinuous orebodies with a tonnage of 1.6 Mt with and average of 49% barite and 10% fluorite (Rajabzadeh, 2007). The ore body ribbon is 0.5 to 4 m thick and extends laterally for approximately 700 m (Fig. 3A). Prior to the main mineralization, carbonate wall rocks underwent pervasive alteration. On the flanks of the mineralized zone, the most common alteration-type is dolomitization (Fig. 4F), overprinted by silicification. The mineralization occurs as massive, banded and laminated types parallel to the host rock strata, replacement of host rock, breccia cement, open-space filling of fractures and dissolution cavities, dissemination, cockade and zebra textures (Fig. 4A-L). The ore minerals are barite, fluorite, and galena, where barite is more abundant than fluorite and galena (Fig. 4G-K). Chalcopyrite and especially pyrite are poorly exposed, being largely oxidized to malachite, azurite, and secondary Fe oxide. Gangue minerals include dolomite, quartz, siderite, calcite, gypsum, and trace amounts of pyrolusite and organic matter (Fig. 4F, J and L). The mineral paragenesis has been previously described by Rajabzadeh (2007). The Nayband Fm. clastic sequence-hosted FBA can be distinguished from the Shotori carbonate-hosted FAB not only by the nature of the host rocks, but also based on the presence of organic matter, clay, higher sulfide contents and rare chlorite.

There were most likely two distinct phases of mineral deposition based upon texture and cross-cutting relationships. Mineralization is thought to have ceased in the intervening period due to probable tectonic uplift with moderate weathering of chalcopyrite and pyrite to malachite and azurite. Broadly, the earliest mineralization (stage-I of sub-economic baritization) includes discontinuous and irregular strata-bounded horizons, commonly >10 cm thick and several tens of meters long (Fig. 4A, B), which developed by barite replacement of fluorite. This observation is in line with a previous study in the Komsheche area (Forghani-Tehrani, 2003). Colorless fluorite was intergrown with quartz and overgrown by barite (Fig. 4C). Medium grained, subhedral, crystalline (>2 mm) aggregates of globular barite, followed by repeated crystallization, include rhythmites of barite-I, siderite, and ferroan sparry dolomite in the dolostone host (Fig. 4D). In this stage, pseudomorphic replacement of layering or pseudo-layering by barite likely reflects the remnant of a host-rock diagenetic texture. The mineralization style of stage-I at Komsheche is similar to that in the Faskhood and Pinavand areas that are hosted by Early Cretaceous successions.

In stage-II, economic baritization formed with less fluorite. Brecciation occurred alternatively along feeder zones and displays a breccia-pipe-like structure (Fig. 4E). The initial breccia appears to be a crackle mineralized-type that laterally grades to pseudo-breccia. Away from the feeder zone, mineralization was likely spatially restricted to dissolution cavities and pores. Stage-II followed with more fluoritization in direct contact with coaly Nayband Fm. Here, breccia with angular siliciclastic rock fragments is cemented by coarse-grained euhedral platy barite, fluorite (white and violet fluorite varieties), and sulfide minerals (Fig. 4I and J). The subsequent phase involved ore reconstitution where pore spaces and breccia cement were occupied by mega-crystals (cm-sized) of tabular barite (generation-III), well-developed cubic fluorite and acicular quartz associated with sub-angular fragments of barite and fluorite, and oxidized sulfide veinlets. Greenish, brown, grey, blue and violet fluorite varieties (generation-III) formed within enclosing rocks at this stage. The latest phase was associated with orbicular-like and cockade textures of secondary barite, fluorite, and silica overgrowths (Fig. 4H, K and L).

Since the types of barite and fluorite crystals vary within the Komsheche deposit, several modes of occurrence are recognized based on morphology, texture, size, and color. Barite grains consist of impure fine- to medium-grained barite-I, pure coarse-grained barite-II, large automorphic barite-III crystals, and secondary barite-IV. Fluorite occurs

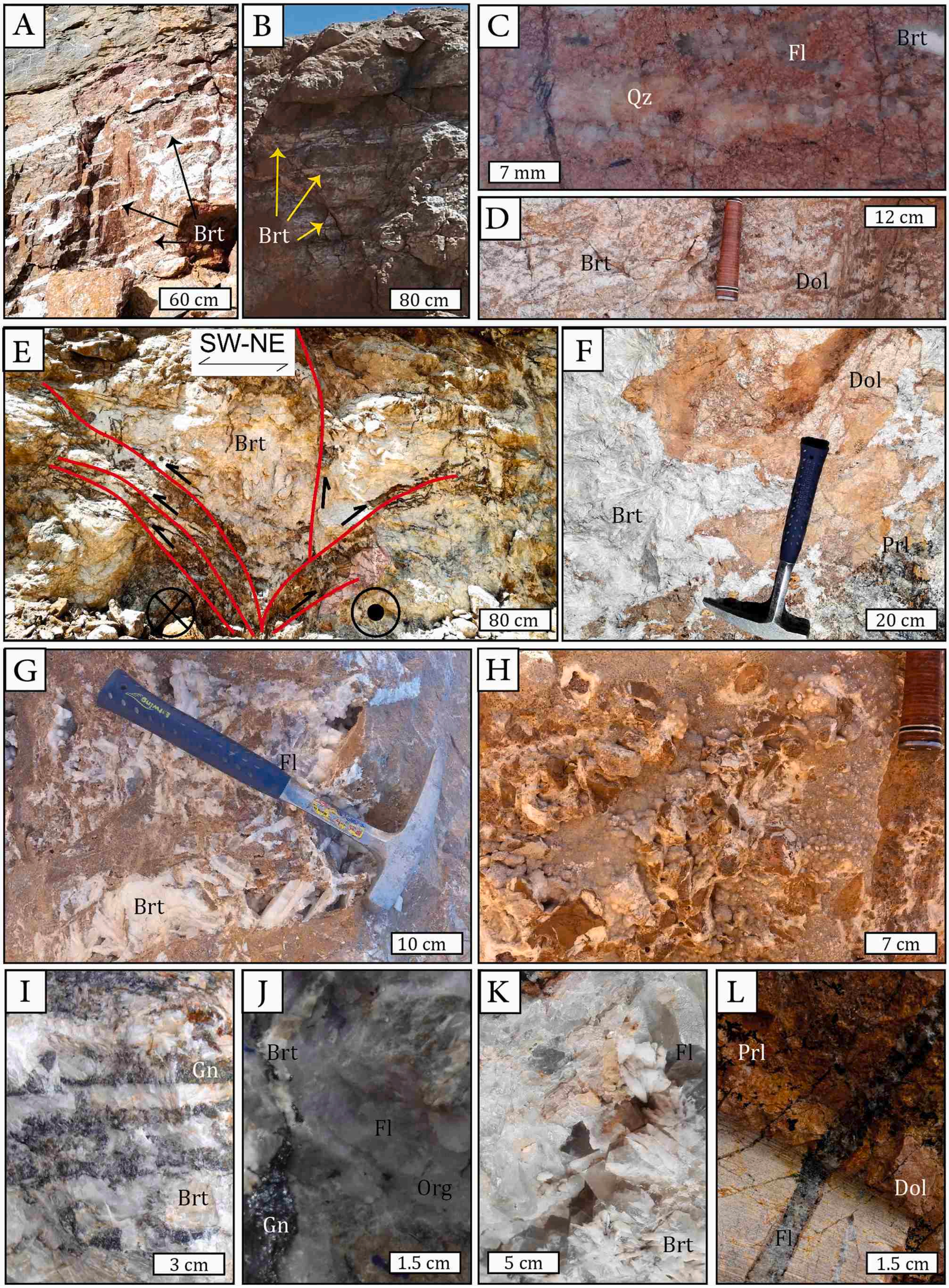

(caption on next page)

Fig. 4. Photographs of various ore textures and structures, all from the Komsheche FBA deposit, except for Fig. A, which is from the Maste-Kuh deposit. (A) Folded Cretaceous limestone with thin white bands of barite. (B) Banded structure with barite, fluorite, and quartz minerals intercalated in the Shotori host dolostone. (C) Cut hand-specimen of the quartz and colorless fluorite bands that were replaced by barite-I. (D) Rhythmic banding of barite globular and ferroan dolomite accompanied by dissolution of carbonate host rock. (E) Hydraulic breccia pipe analogue, sharply bounded by positive flower structure in Triassic strata consisting of brown cm-sized sub-angular fragments of dolomite and siderite associated with early banded barite in a white coarse-grained barite cement. (F) Hydrothermal dolomite formed prior to irregular replacement of dolostone by coarse-grained barite-II. (G) Pseudo-breccia with fractures filled by well-developed fluorite, mega-crystal barite-III, quartz and ferroan dolomite. (H) Cockade of fine-scale banded quartz and secondary barite-IV with clear dissolution of host rock. (I) Zebra texture showing the galena replacement of laminated barite. (J) Fragments of silicified Shemshak Fm. preserved in a matrix of barite, fluorite, quartz, and galena (hand specimen). (K) Drusy barite, large automorphic fluorite and siderite fill karst cavities. (L) Late vein of fluorite cutting dolomite. Abbreviations of Whitney and Evans (2010): Brt-barite, Dol-dolomite, Fl-fluorite, Gn-galena, Org-organic matter, Prl-pyrolusite, and Qz-quartz.

as colorless small to medium interstitial grains of fluorite-I, medium- to coarse-grained multi-colored fluorite-II in cement of the matrix-supported breccias, in some places associated with sulfides, fluorite-III with simple hexahedron green to violet crystal aggregates and, finally, stripped and saccharoidal fluorite-IV as microbands of fluorite.

4. Materials and methods

In this study, brittle and ductile structures were measured and structural analyses were performed to find the linkage between tectonic structures and FBA mineralization. Structural analyses were focused on the Triassic to Cretaceous sedimentary strata hosting barite and fluorite mineralization. The kinematics of fault slip were mainly identified based on classical criteria on polished fault surfaces (e.g., Petit, 1987; Fossen, 2010). Structural analysis consisting of paleostress inversion and statistical analysis of the measured fault slip and bedding data, respectively, were performed with the Windows program DAISY v5.3 (Salvini et al., 1999) in order to obtain the paleostress directions of the region through time. Furthermore, a NE-SW- trending structural cross section, oblique to the general trend of the study area, has been drawn upon the measured structural data to illustrate the relation between ore body and structural architecture of the Komsheche mine.

Isotopic compositions of galena, barite, and fluorite minerals were performed in three laboratories of the University of Oslo (Norway), Ohio State University (USA), and Universidad Nacional Autónoma de México (Mexico).

Seven representative fluorite samples (a variety of textures including replacement, breccia cement, and open-space filling) were chosen for geochemical analysis. Fluorite samples Z-1 and Z-3 were associated with galena. The concentration of rare earth elements (REE) and other trace elements of pure fluorite samples were determined by ICP-MS analysis at Actlabs Laboratories, Ancaster, Ontario, Canada. These fluorite samples were investigated for (U-Th)/He low-temperature thermochronology with a closure temperature window, still poorly understood, of about 50 to 170 °C (90±10 °C, Evans et al., 2005; 46 ± 14 °C and 169 ± 9 °C, Wolff et al., 2016). In all cases U and Th concentrations were less than 1 ppm, making it difficult to obtain a good age determination.

Two galena samples were analyzed for lead isotopes. The lead was leached from the samples with dilute acid, mixed with phosphoric acid and silica gel, and loaded on outgassed Re filaments. Ratios were measured by thermal ionization mass spectrometry on a MAT262 instrument using multiple Faraday cups in static mode. Data are corrected for fractionation by 0.10 ±0.06 % per atomic mass unit. The reproducibility of the fractionation (based on NBS982) is propagated into the uncertainty of the corrected ratios. Isoplot Windows program is used for the statistical calculation of the Pb-Pb isotopes to obtain the age modeling trend.

In order to measure $^{87}Sr/^{86}Sr$, five barite specimens were collected. After petrographic observation, pure barites were crushed by hand and carefully handpicked under a binocular microscope to remove the impurities. Then, ~10 mg of each barite sample was dissolved by chelation with cation exchange resin following Paytan et al. (1993). The bulk dissolved samples were passed through a column with Sr-specific resin (Scher et al., 2014), separating Sr. Strontium was loaded onto single rhenium-filaments with a Ta activator solution using the sandwich technique. Isotopic ratios were then analyzed using a Thermo Fisher Scientific Triton Plus multicollector thermal ionization mass spectrometer. Isotopic ratios are corrected for instrumental mass fractionation by normalizing to $^{88}Sr/^{86}Sr = 8.3752$. The isotopic ratio external uncertainty is estimated using replicate analyses of SRM 987 as 0.000008 (2σ). Three analyses of SRM 987 yielded an average value of 0.710254, within uncertainty of the accepted value for SRM 987 (0.710248; McArthur et al., 2012). One sample was prepared twice (from two different aliquots of the powdered barite samples). The difference between the two is 0.000006, less than the external uncertainty of the SRM 987.

5. Results

5.1. Structural evidence

A detailed and original structural survey and geological mapping were undertaken to decipher the structural architecture of the Komsheche deposit, as described in the following paragraphs and Figs. 3A, B and 5. The study area, located just west of the active trace of the ZFS, has been intensely affected by brittle and ductile deformation (Fig. 2). The structural measurements and cross-cutting relationships in the deposit and surrounding area indicate two distinct generations of brittle structures (mainly faults, fractures and veins), which are recognized where the new generation cut the old generation.

The first generation structures were developed by (i) a major NE-dipping reverse fault in the center of the deposit that thrust the FBA-bearing Triassic carbonates over the Nayband Fm. (Fig. 5F). The kinematics of this fault are recognized based on vertical slickenlines and synthetic Riedel shears on the polished fault surfaces with NE-ward verging synclines, drag folds, in the footwall (Fig. 5F). (ii) The NE-SW trending, and both NW and SE - dipping, extensional faults cut the Triassic and Cretaceous carbonates. Those are mostly exposed in the central mine showing few meters of vertical offsets (Figs. 4B, 5A and 5B). The kinematics of these faults are identified based on vertical slickenlines and synthetic Riedel shears on the polished fault surface (Figs. 3B, 5B, and Table 2). The normal faults have widths of about one meter and are associated with breccia, barite, and fluorite (Fig. 5A-D). (iii) The NE-SW trending FBA-bearing veins vary in length and width (Fig. 5B).

Second generation-related structures are manifested by (iv) a steeply dipping, NW-SE striking right-lateral strike-slip fault, sub-parallel to the ZFS. It runs from north to east across the Komsheche quarry, cutting through the Cretaceous carbonates and a Quaternary stream that made ca. 420 m right-lateral displacement in Cretaceous carbonate in the north (Figs. 2 and 3A). To the northeast, there are (iv) N-S trending extensional faults that mostly emerge in Cretaceous strata with tens of meters vertical offsets (Figs. 3A and 5G), and (v) sub-vertical N-S trending veins with different length and width, dominantly filled by barite and fluorite (Fig. 4 and Table 2). Regarding the ductile deformation, a general NW-SE folding axis can be identified in the Komsheche mine area (Fig. 3A). In the regional scale, two different fold trends NW-SE and E-W can be distinguished (Fig. 2). Bedding measurements reveal a major NW-SE trending fold axis and a minor E-W trending fold axis (Fig. 3A).

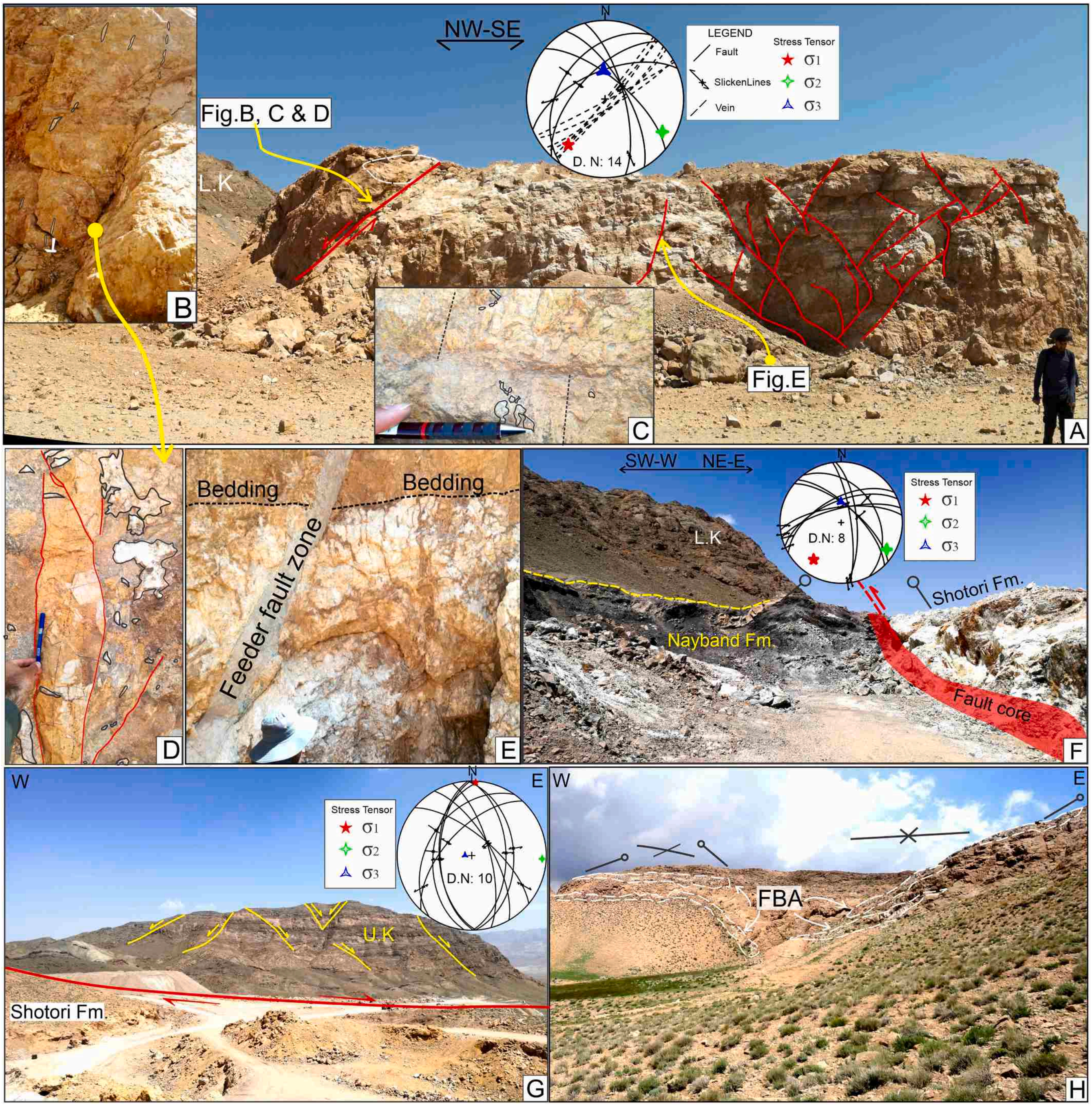

Fig. 5. (A) Panoramic view showing the FBA-bearing Shotori Fm. that is cut by NE-SW tending extensional fault zones. Red lines indicate the faults. Stereoplot (Schmidt net, lower hemisphere projection) represents collected brittle structures data and its paleostress inversion result. (B) Sub-vertical NW-dipping extensional fault cuts through the Shotori Fm. with about 1 m vertical displacement and FBA mineralization in both footwall and hanging wall. For location see Fig. 3A. (C) Close view of the polished fault surface of the NW-dipping extensional fault with vertical slicken-line and downward step, and remnants of the FBA mineralization on the fault surface. For location see Fig. 3A and B. (D) Breccia and intact generations (types/forms) of FBA mineralization within the meso-scale view of the NW-dipping extensional fault zone. Red lines showing the fault and fractures. For location see Fig. 3A. (E) Layer-like FBA mineralization confined by carbonate bedding boundaries and fed by an oblique feeder fault zone. For location see Fig. 3A. (F) Panoramic view showing the NW-SE striking NE-dipping fault that thrusts the Shotori Fm. over the Nayband Fm. and Cretaceous strata, causing the footwall syncline. Stereoplot (Schmidt net, lower hemisphere projection) represents brittle structures and their paleostress inversion result. (G) Second generation steep N-S trending extensional faults just to the north of Komsheche active deposit cutting through the Cretaceous carbonates. Stereoplot (Schmidt net, lower hemisphere projection) represents collected brittle structures data and the paleostress inversion result. (H) Roughly E-W trending folds in layer-like FBA bearing Early Cretaceous limestone (rudist-bearing) strata, about 1 km north of the Komsheche mine, see Fig. 2 for location. Abbreviation for Fig A, F, and G: L.K - Lower Cretaceous, U.K - Upper Cretaceous.

Table 2
Measured structural data in Komsheche FBA mine area.

Site	Latitude	Longitude	Lithology	Age of Formation	Strike	Dip	Rake	Kinematic	Element
1	33°13′2″N	52°2′2″E	Limestone	Lower Cretaceous	303	35			Bedding
2	33°13′0″N	52°2′23″E	Carbonate	Triassic	215	41	89	Normal	Fault
2	33°13′0″N	52°2′23″E	Carbonate	Triassic	37	53	83	Normal	Fault
2	33°13′0″N	52°2′23″E	Carbonate	Triassic	310	68	82	Reverse	Fault
2	33°13′0″N	52°2′23″E	Barite		60	88			Vein
2	33°13′0″N	52°2′23″E	Barite		62	87			Vein
2	33°13′0″N	52°2′23″E	Barite		48	90			Vein
2	33°13′0″N	52°2′23″E	Barite		51	89			Vein
2	33°13′0″N	52°2′23″E	Barite		40	79			Vein
2	33°13′0″N	52°2′23″E	Barite		38	83			Vein
2	33°13′0″N	52°2′23″E	Barite		42	85			Vein
2	33°13′0″N	52°2′23″E	Barite	Triassic	240	57	10	Sinistral	Vein
3	33°13′3″N	52°2′33″E	Dolomite	Triassic	345	52			Bedding
3	33°13′3″N	52°2′33″E	Shale	Triassic	310	45			Bedding
3	33°13′3″N	52°2′33″E	Dolomite	Triassic	330	70	83	Reverse	Fault
3	33°13′3″N	52°2′33″E	Dolomite	Triassic	345	70	79	Reverse	Fault
4	33°13′14″N	52°2′20″E	Limestone	Cretaceous		37			Bedding
5	33°13′19″N	52°3′10″E	Limestone	Cretaceous	327	31			Bedding
5	33°13′19″N	52°3′10″E	Limestone	Cretaceous	356	57	87	Normal	Fault
5	33°13′19″N	52°3′10″E	Limestone	Cretaceous	183	51	88	Normal	Fault
6	33°13′31″N	52°3′05″E	Limestone	Cretaceous	319	29			Bedding
6	33°13′31″N	52°3′05″E	Limestone	Cretaceous	178	61	83	Normal	Fault
6	33°13′31″N	52°3′05″E	Limestone	Cretaceous	358	62	89	Normal	Fault
7	33°13′24″N	52°3′06″E	Limestone	Cretaceous	171	55	76	Normal	Fault
7	33°13′24″N	52°3′06″E	Limestone	Cretaceous	169	59	77	Normal	Fault
8	33°13′02″N	52°2′34″E	Barite		171	81			Vein
8	33°13′02″N	52°2′34″E	Barite		179	79			Vein
8	33°13′02″N	52°2′34″E	Barite		183	88			Vein
8	33°13′02″N	52°2′34″E	Barite		190	85			Vein
8	33°13′02″N	52°2′34″E	Barite		185	83			Vein
9	33°12′57″N	52°2′37″E	Dolomite	Triassic	297	76	155	Dextral	Fault
9	33°12′57″N	52°2′37″E	Dolomite	Triassic	301	75	156	Dextral	Fault
10	33°12′43″N	52°2′11″E	Limestone	Cretaceous	127	38			Bedding

The FBA mineralization occurs dominantly as conformable layers confined within the bedding of carbonate strata and breccias. The banded-type FBA mineralization occurs between major steep extensional fault zones in Triassic carbonate strata (Figs. 3A, 5A and 5H). By contrast, the breccia-type FBA mineralization is almost entirely confined to fault zones (Figs. 5B and 5D), which also contain the euhedral/ intact-type (Fig. 5D).

5.2. *Geochemistry and (U-Th)/He age of fluorite*

5.2.1. *Trace and REE contents*

Table 3 displays trace elements analyses, together with detection limits, of seven dated fluorite separates (grains, Fig. 6). The elements Ag (<0.5 ppm), Cr (<20 ppm), Cs (<0.1 ppm), In (<0.1ppm), Ga (<1ppm), Ge (<0.5 ppm), Mo (<2 ppm), Ni (<20 ppm), Tl (<0.05 ppm), V (<5 ppm), and Zn (<30 ppm) from all the studied fluorites have concentrations below the detection limits stated and were not included in Table 3. Most of these elements were not expected in any measurable amount in fluorite, but it is important to report them because they can be associated to inclusions of sulfides and other minerals, which are not present. The fluorite has low amounts of most analyzed trace elements, except Ba (110-94000 ppm), Sr (47-2410 ppm), and Pb (6-6780 ppm). The mean total REE and yttrium (REY) content of the fluorites is low (15.78 ppm). Variable colors do not correlate with different compositions, with the exception of cloudy violet fluorites, which are associated with galena and have higher Pb abundances (samples Z-1, Z-2 and Z-3 in Table 3 and Fig. 6). The fluorites show positive anomalies for Ba, Pb, Sr, U, Ta, and Y and negative anomalies for Rb, Th, La, Pr, Ce, and Nd when examined in an Upper Continental Crust - normalized diagram (Fig. 7A). The chondrite-normalized REY patterns, obtained using values of Anders and Grevesse (1989), have a subhorizontal shape with a negative slope of the heavy rare earth elements (HREE). There is a positive Y anomaly, but almost negligible Eu and Ce anomalies (Fig. 7), indicating a range of 0.54 to 0.99 with mean value ~0.8 for $Eu/Eu^{*}=Eu_n/\sqrt{[Sm_n \times Gd_n]}$ (except for samples Z-1 and Z-2 with ratios 1.01 and 1.23), and a range of 0.56 to 0.99 mean value ~0.8 for $Ce/Ce^{*}=Ce_n/\sqrt{[La_n \times Pr_n]}$ (except for sample Z-6 with ratio 1.02) (Table 3). However, sample Z-7 has more pronounced negative anomalies for Ce and Eu (Fig. 7B).

The REE patterns of Komsheche fluorites can be divided into two groups. The first group (polycrystalline fluorite samples Z-1, Z-3 and Z-7 collected/selected from matrix-supported breccia cement; dashed red lines in Fig. 7B), present weakly increasing abundances from La to Eu, slightly enrichment of the MREE, decreasing abundances from Eu to La (dashed lines in Fig. 7B), and a low La/Lu ratio. By contrast, the second group (coarse-grained fluorite samples Z-2, Z-4, Z-5 and Z-6) is slightly enriched in LREE rather than MREE concentrations (solid lines in Fig. 7B).

5.2.2. *(U-Th)/He ages of fluorite*

Measurements of U, Th, and He were made on all seven fluorite samples whose description has already been presented in section 4. The macroscopic characterization (color and texture) of Komsheche fluorites are also shown in Fig. 6 and Table 4. Fluorite ages range from 437.6 to 4.6 Ma, although most are Cenozoic. As stated before, the most probable cause of this large scatter is the very low content of both U and Th and their probable inhomogeneous distribution in the studied samples. Any attempt to systematize the data is a complicated task but two main age groups seem to be present: Cretaceous and Eocene to Miocene. Sample Z-7 gives an unrealistic Paleozoic age, probably related to the presence of helium in fluid inclusions, a point that has not been verified. It is noteworthy that there is some correlation between the Sr contents and the (U-Th)/He ages, except for sample Z-5 that has a high Sr concentration perhaps due to the presence of carbonate contamination. This correlation can indicate that “older” samples are indeed associated to first stages of carbonate replacement. A correlation between Sr and age

Table 3
Composition of fluorite samples from Komsheche deposit.

Sample no.		Z-1	Z-2	Z-3	Z-4	Z-5	Z-6	Z-7
Color	detection limit	cloudy violet	dark violet	cloudy violet	pale violet	white to green	green to violet	colorless
Zr	1	<1	4	<1	<1	1	1	<1
Y	0.5	15.3	2.6	3.4	11.1	12.0	12.0	12.3
Nb	0.2	1.1	2.0	0.9	0.9	0.7	0.8	0.7
Co	1	2	2	2	2	2	2	2
Ba	3	4640	428	192	110	94000	4000	54400
Rb	1	<1	2	<1	<1	<1	<1	<1
Sr	2	156	65	206	47	2410	119	861
Cu	10	10	30	40	20	20	30	20
Pb	5	268	178	6780	<5	6	9	30
As	5	<5	5	8	5	<5	<5	<5
Bi	0.1	<0.1	0.1	<0.1	<0.1	0.1	0.2	0.8
Ga	1	<1	1	<1	<1	<1	<1	<1
Hf	0.1	0.1	0.1	<0.1	<0.1	0.1	<0.1	0.1
Sb	0.01	2.3	4.1	17.9	0.8	9.4	42.9	2.7
Sn	1	1	2	2	4	<1	<1	<1
Ta	0.01	0.44	0.52	0.39	0.41	0.39	0.39	0.39
Th	0.05	0.35	0.38	0.18	0.06	0.05	0.07	0.2
U	0.01	0.36	0.39	0.07	0.18	0.22	0.30	0.62
W	0.5	<0.5	<0.5	<0.5	<0.5	2.5	<0.5	<0.5
La	0.05	0.43	0.21	0.13	0.68	1.07	0.82	0.42
Ce	0.05	1.28	0.42	0.34	2.11	1.76	2.59	0.50
Pr	0.01	0.25	0.06	0.06	0.38	0.32	0.45	0.11
Nd	0.05	1.64	0.35	0.52	2.21	2.10	2.64	0.75
Sm	0.01	0.64	0.12	0.20	0.57	0.67	0.72	0.43
Eu	0.005	0.294	0.070	0.069	0.225	<0.005	0.240	0.116
Gd	0.01	1.21	0.25	0.29	0.83	1.13	0.89	0.98
Tb	0.01	0.19	0.03	0.04	0.11	0.12	0.12	0.13
Dy	0.01	0.99	0.17	0.19	0.53	0.50	0.58	0.69
Ho	0.01	0.17	0.03	0.03	0.09	0.08	0.09	0.13
Er	0.01	0.41	0.08	0.06	0.19	0.17	0.19	0.29
Tm	0.005	0.045	0.008	0.007	0.018	0.017	0.020	0.027
Yb	0.01	0.18	0.03	0.03	0.08	0.06	0.07	0.14
Lu	0.002	0.017	0.004	<0.002	0.008	0.006	0.008	0.190
Eu/Eu*	-	1.014	1.227	0.870	0.993	-	0.910	0.543
Ce/Ce*	-	0.935	0.897	0.922	0.995	0.721	1.022	0.558

has already been observed by Pi et al. (2004) in the carbonate-hosted hydrothermal fluorite mineralizations of Taxco, Mexico.

5.3. *Pb and Sr isotopic composition of galena and barite minerals*

5.3.1. *Lead isotopes*

Analyses of the two galena samples are relatively homogeneous with ^{206}Pb/^{204}Pb ratios of 18.591 and 18.540, ^{207}Pb/^{204}Pb of 15.725 and 15.693, and ^{208}Pb/^{204}Pb of 38.730 and 38.594 (Table 5). Pb isotopic ratios of MVT deposits on comparable structural zones of Iran, south China and Tunisia are in the Table 5. The data plot above the crustal Pb growth curves of Stacey and Kramers (1975) in both diagrams (Fig. 8A, B). They are slightly shifted towards higher ^{207}Pb/^{204}Pb than the Pb isotopic compositions of Central Iran (Fig. 8A) and fall between the lower crust and orogenic lead, but closer to the orogen curve (Fig. 8B). The Pb-Pb model age for the Komsheche galenas is ~110 Ma (highest stage in the Early Cretaceous).

5.3.2. *Strontium isotopes*

Strontium isotope analyses conducted on barite samples from the breccia cement (type-II) and the open-space filling (type-III) are presented in Table 6. Pure barite separates from this study range from 0.709147 to 0.709595, higher than Triassic dolomitic host rock (Sr isotopic record ~ 0.70726 to 0.70825; Korte et al., 2003), Cretaceous sediments (~ 0.7071 to 0.7078; see McArthur et al., 2001), and Miocene marine Sr (~ 0.708255 to 0.709027; McArthur et al., 2001) (Fig. 9). The comparison of Sr isotopes ratios from barites of Komsheche and Irankuh Zn-Pb±Ba deposits to the Mesozoic host rock, hydrothermal calcite of Ab-Bagh Zn-Pb±Ba deposit, Paleozoic seawater, Miocene seawater, and Miocene granodiorite is shown in Fig. 9. Sample KB-1, collected at the direct contact with Nayband dark shale, is significantly more radiogenic than other samples. As represented in Fig. 9, in respect to the ages of host rock and mineralization, the ^{87}Sr/^{86}Sr values of barite samples imply that their Sr is not derived from Mesozoic seawater. Sample KB-2 of generation-III has a Sr ratio closest to that of Miocene seawater (Fig. 9).

6. Discussion

6.1. *Structural evolution of the Komsheche area*

Following the Cretaceous, a NE-SW-directed extensional regime initiated the Abbas-Abad Fault and ZFS and led to the unconformable deposition of a rift-related thick pile of carbonates over the older strata (Safaei et al., 2008; Tabaei et al., 2016). The subsequent poly-phase contractional deformation that occurred in the region is reconstructed in the following section.

Paleostress, derived from our local structural measurements, is integrated with the regional structural architecture and with published data to reconstruct the long-term structural evolution of NE Isfahan. According to the widespread NW-SE and roughly E-W trending fold trends (Fig. 2), two distinct NE-SW and approximately N-S maximum compression directions are suspected. The outputs of the paleostress inversion analyses on the measured brittle structures reveal a NE-SW (strike of N048, 12) and a roughly N-S (strike of N007, 10) maximum compression direction (Figs. 5A, F and G). Furthermore, the cross-cutting relationship between faults imply that the structures that propagated under the N-S directed maximum compression direction cut through the structures that accommodated the NE-SW directed maximum compression direction. In turn, it is in line with the overprinting of the roughly E-W trending folds on the NW-SE trending folds (Figs. 2 and 3A).

Both structure generations overprint all the stratigraphic units of the

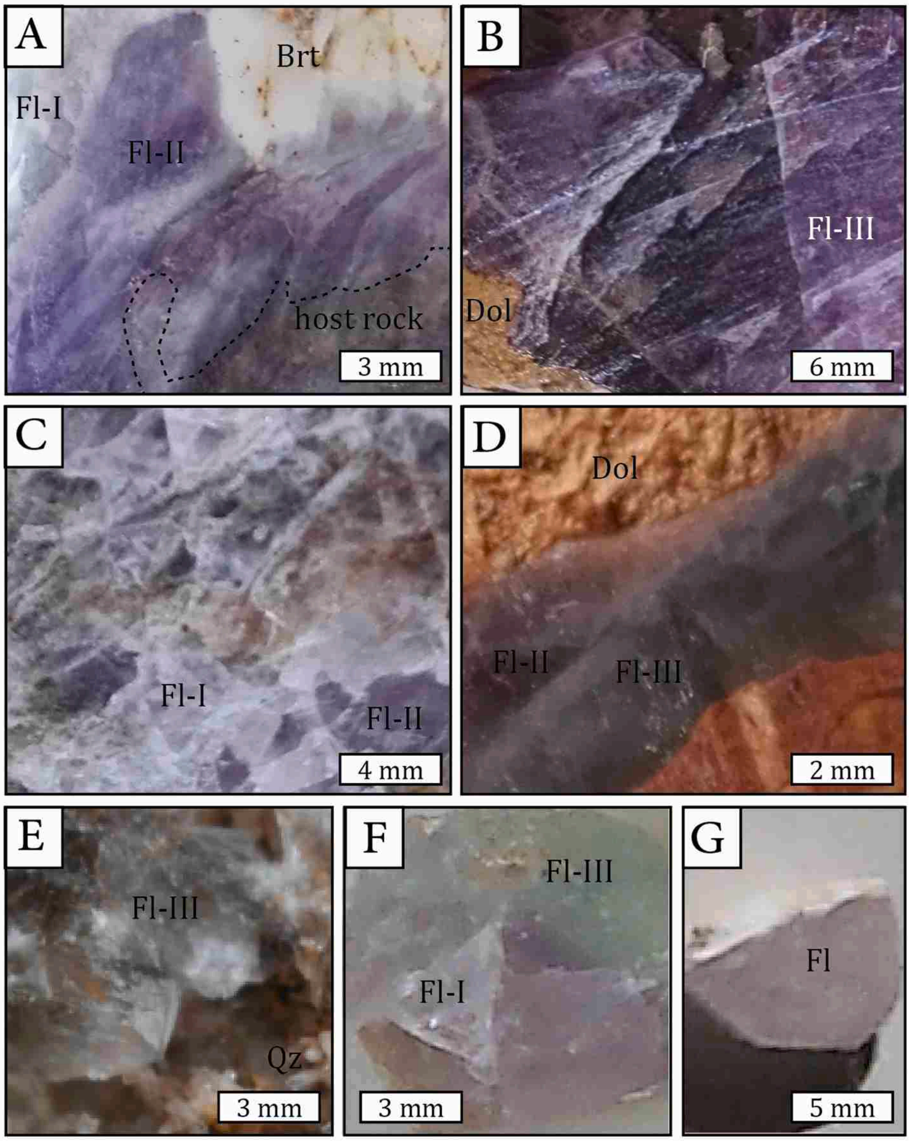

Fig. 6. Photographs of the representative morphologies and textural characteristics of the seven studied fluorite samples from the Komsheche deposit. (A) Host rock cemented by fluorite and barite. Sample Z-1 displays recrystallized texture of the violet fluorite-II around the colorless subhedral fluorite crystal Fl-I. (B) In sample Z-2, coarse-grained hypidiomorphic fluorite-III occurs as vein filling in host dolostone. (C) Sample Z-3 is part of a vein breccia in which colorless fluorite-I alternates with violet and brown fluorites. (D) Coarse-grained fluorite-III after fluorite-II of sample Z-4, observed as a late-phase filling in the dolomite. (E) Large euhedral crystals of fluorite-III and acicular aggregates of quartz occur as cavity-filling in sample Z-5. (F) In sample Z-6 coarse-grained fluorite-III followed fluorite-I. (G) Medium-grained colorless fluorite in sample Z-7.

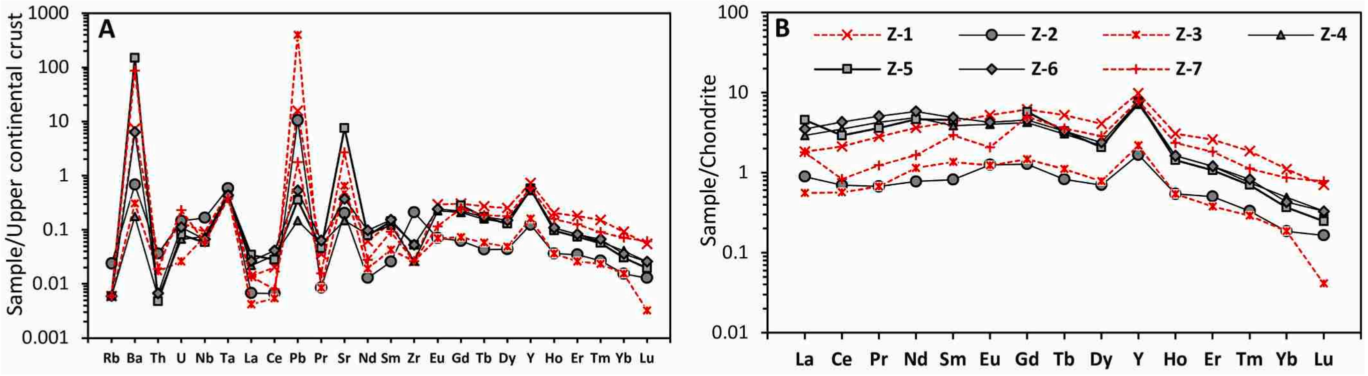

Fig. 7. Multi-elements and REE diagrams for the Komsheche fluorite samples. Normalizing values for upper continental crust (A) and C1 chondrite (B) are from Rudnick and Gao (2003) and Anders and Grevesse (1989), respectively. Symbols of A and B are the same.

Komsheche area, hence it can be inferred that both compressive regimes are post-Cretaceous. In order to assign a rough age to these compressional tectonic regimes, we further examine the complete stratigraphic sequence preserved south, north, and northeast of the study area (Fig. 2). To the south, all the Mesozoic and Paleogene stratigraphic units were deformed by the NW-SE and N-S directed compression events (Radfar et al., 1999). The Eocene rock units to the north of Komsheche show a NW-SE trending fold axis (Fig. 2) (Radfar et al., 1999). To the east, south of Ardestan, the

Table 4
(U-Th)/He results of seven dated fluorite samples from the Komsheche FBA deposit.

Sample no.	Textural type	REE (µg/g)	Sr (µg/g)	U (µg/g)	Th (µg/g)	^{4}He (mol/g)	Age (Ma)
Z-1	Carbonate replacement, breccia cement	23.05	156	0.36	0.35	3.30×10^{-10}	137
						1.02×10^{-10}	42.6
Z-2	Late vein	4.43	65	0.39	0.38	4.87×10^{-11}	18.8
						3.91×10^{-11}	15.1
Z-3	Carbonate replacement, breccia cement	5.37	206	0.07	0.18	7.33×10^{-11}	120
						1.59×10^{-09}	-
Z-4	Late vein	19.13	47	0.18	0.06	1.62×10^{-11}	15.5
						3.04×10^{-11}	29.0
Z-5	Large open-space filling	20.01	2410	0.22	0.05	5.70×10^{-12}	4.6
						3.80×10^{-11}	30.4
Z-6	open-space filling and replacement	21.43	119	0.30	0.07	1.11×10^{-11}	6.5
						1.12×10^{-10}	65.5
						1.96×10^{-11}	11.5
Z-7	Carbonate replacement	17.03	861	0.62	0.20	1.64×10^{-09}	438

Table 5
Pb-Pb data of galena from the Komsheche deposit (this work) and compiled data from other structural zones of Iran, south China, and northeast Tunisia.

Location	Sample no.	^{206}Pb/^{204}Pb	2σ (%)	^{207}Pb/^{204}Pb	2σ (%)	^{208}Pb/^{204}Pb	2σ (%)	Reference
Komsheche	KG-5	18.591	0.06	15.725	0.06	38.730	0.06	this study
	KG-6	18.540	0.06	15.693	0.06	38.594	0.06	
Central Iran	Qullehkaftaran	18.461	0.004	15.586	0.004	38.50	0.011	Mirnejad et al. (2011)
	Nakhlak	18.511	0.005	15.637	0.005	38.642	0.013	
	Nakhlak	18.516	0.002	15.638	0.002	38.641	0.006	
	Chahsorb	18.427	0.004	15.647	0.004	38.575	0.012	
	Kamar-Mehdi	19.081	0.003	15.722	0.003	38.910	0.009	
	Geijerkuh	18.514	0.003	15.704	0.004	38.696	0.013	
	Mehdi-Abad	18.499	0.003	15.658	0.003	38.634	0.010	
Alborz	Bala-Kuh	18.505	0.005	15.618	0.005	38.593	0.014	Mirnejad et al. (2011)
	Erambozorg	18.505	0.007	15.629	0.006	38.583	0.018	
	Pachi-Miana	18.598	0.003	15.655	0.003	38.632	0.008	
	Ahvano	18.404	0.002	15.639	0.003	38.538	0.008	
Sanandaj-Sirjan	Ahangaran	18.407	0.003	15.641	0.003	38.571	0.011	Hosseinkhani and Molasalehi (2013)
	Emarat	18.62	-	15.64	-	39.14	-	Ehya et al. (2010)
	Emarat	18.57	-	15.77	-	39.22	-	
	Emarat	18.58	-	15.68	-	39.21	-	
	Emarat	18.56	-	15.65	-	39.98	-	
	Emarat	18.45	-	15.58	-	38.69	-	
	Emarat	18.55	-	15.57	-	38.64	-	
	IranKuh	18.45	-	15.65	-	38.62	-	Karimpour and Sadeghi (2011)
South China	Dong Li	18.19	-	15.75	-	38.45	-	Schneider et al. (2002)
	Lomichang	18.18	-	15.75	-	38.43	-	
	Lomichang	18.19	-	15.76	-	38.47	-	
	Lomichang	18.19	-	15.75	-	38.47	-	
	Ma Chang-Banpo	18.18	-	15.74	-	38.42	-	
	Paiwu	18.21	-	15.77	-	38.52	-	
Northeast Tunisia	Hamman Zriba	18.87	-	15.68	-	38.75	-	Jemmali et al. (2017)
	Hamman Zriba	18.87	-	15.68	-	38.74	-	
	Hamman Zriba	18.80	-	15.66	-	38.68	-	
	Hamman Zriba	18.87	-	15.68	-	38.73	-	
	Hamman Zriba	18.86	-	15.68	-	38.74	-	
	Hamman Zriba	18.87	-	15.68	-	38.75	-	

Oligocene and Oligo-Miocene units are tightly folded in a NW-SE trending style, while northwest of Ardestan the Miocene strata clearly are folded with a E-W trend (Fig. 2) (Radfar et al., 1999). Based upon the correlation between the stratigraphic ages of the folded units and two NW-SE and E-W distinct folding styles, it can be inferred that a shift in the maximum compression direction from NE-SW to ~ N-S has occurred at least after the Middle Miocene. This proposed time for the tectonic shift is consistent at the scale of the overriding plate of the Zagros orogeny, as our paleostress results are comparable with the paleostress results obtained for the ZFS, the SaS, the CEIM, and the Zagros fold and thrust belt (Navabpour et al., 2007; Tadayon et al., 2017, 2019; Salehi and Tadayon, 2020; Alaminia et al., 2020). Furthermore, it is worth noting that a short-lived NE-SW-directed extensional regime acted on the region during a Late Oligocene to Early Miocene time-lapse (Reuter et al., 2007; Morley et al., 2009; Alaminia et al., 2020).

6.2. *Possible source-rocks of Pb, Sr, and S in the Komsheche deposit*

Lead isotopic compositions of Komsheche galena clearly indicate an upper crustal source with multistage lead components similar to Pb isotope ratios in the Malayer-Isfahan Pb-Zn belt (Karimpour and Sadeghi, 2018). The calculated model age suggests that galena could have formed by the remobilization of lead from a crustal reservoir in the uppermost of Early Cretaceous. The data show a close similarity to the Pb signature in other domains of Central Iran, Alborz, and SaS zone (Fig. 8).

The ^{87}Sr/^{86}Sr ratios are a useful tool to record the original values of fluid pathways and sources for barite formation (Reesman, 1968; Paytan et al., 2002; Kraemer et al., 2019), although the deviating isotopic composition of the mineralizing fluid is related to the water-rock interaction processes (Piqué et al., 2008; Lepetit et al., 2019). The

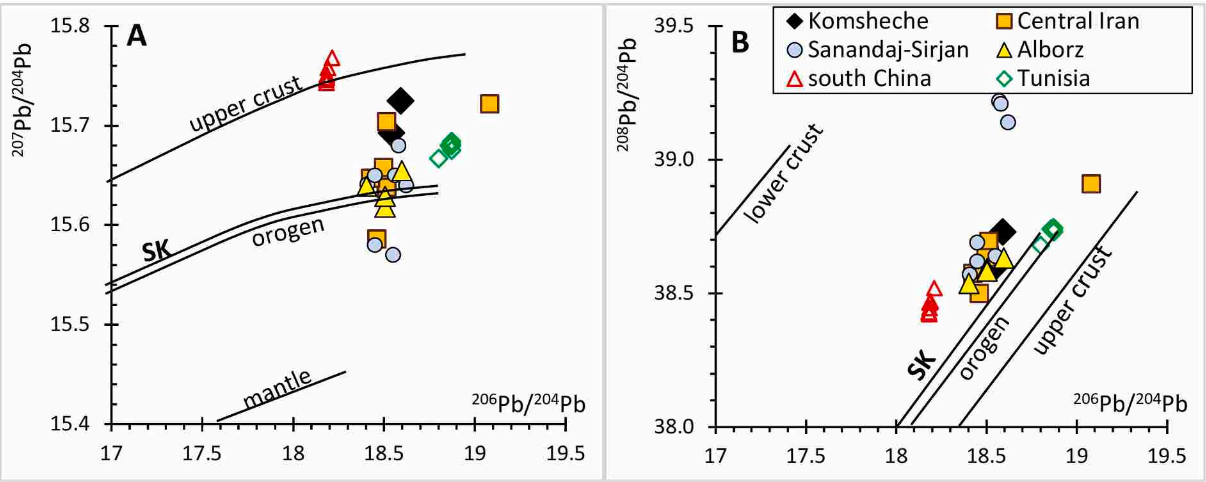

Fig. 8. Plots of Pb isotope composition of galena from the Komsheche mine. (A) ^{207}Pb/^{204}Pb versus ^{206}Pb/^{204}Pb diagram, and (B) ^{208}Pb/^{204}Pb versus ^{206}Pb/^{204}Pb diagram. Trends of Pb isotope ratios are from plumbotectonic model of Zartman and Doe (1981) and the average crustal growth curve (SK curve) is from Stacey and Kramers (1975). See the Table 5 for detail.

Table 6
Strontium isotope composition of Komsheche barite samples (this study) and Irankuh deposit (Ghazban et al., 1994).

Location	Sample no.	Generation	^{87}Sr/^{86}Sr	±2σ
Komsheche	KB-1	II	0.709595	0.000006
	KB-2	III	0.709147	0.000006
	KB-3	II	0.709222	0.000006
	KB-3 duplicate	II	0.709216	0.000008
	KB-4	II	0.709198	0.000006
	KB-5	II	0.709195	0.000008
Irankuh	Brt-L2-5-2		0.70839	-
	Brt-L-4-3		0.70864	-
	Brt-MOL-3		0.70845	-
	Brt-BM-4-2		0.70878	-
	Brt-BM-7-4		0.70846	-

Komsheche barites display a narrow range of ^{87}Sr/^{86}Sr from 0.70915 to 0.70960. These Sr isotopic compositions are more radiogenic than those of Mesozoic seawater (Triassic, Jurassic, and Cretaceous seawater compositions; 0.70677 to 0.70778, 0.70690 to 0.70794 and 0.70710 to 0.70775, respectively; Burke et al., 1982; Koepnick et al., 1990). It should be noted that the slightly decreasing Sr isotopic compositions from type-II to type-III in the Komsheche barites would be compatible with a mixed source of seawater Sr and older crust (Fig. 9). These ratios probably indicate fluids that interacted with rocks containing more radiogenic minerals. Decomposition of K feldspar and mica is most likely the source of this radiogenic Sr. For instance, the altered Jurassic dark coaly shale from the Irankuh deposit has Sr ratios ranging from 0.719 to 0.726 (Ghazban et al., 1994), much higher than those measured in Mesozoic seawater (Fig. 9). Also, Early Triassic red beds of SW Germany yielded ^{87}Sr/^{86}Sr ratios around 0.709 (Ufrecht and Hölzl, 2006) higher than seawater. Hence, the higher ^{87}Sr/^{86}Sr ratios at Komsheche may be explained by diverse sources of the ore-forming fluids, including three end members of (A) a surficial and cool water of Miocene seawater or shallow sediment, (B) altered Late Triassic Nayband shales and sandstones or even Early Cretaceous red beds evaporites, and (C) a deep and closed system reservoir of hot basinal fluid leaching the Paleozoic basement (^{87}Sr/^{86}Sr~0.7067 to 0.7091; Burke et al., 1982). It is reasonable to assume that the fluids were derived primarily from basinal brines trapped within Paleozoic basement, which has a relatively similar Sr isotopic composition as the Komsheche barites (see Fig. 9). During the subsequent migration along unconformities and faults the fluids mixed with minor amounts of water leached from the Mesozoic siliciclastic rocks or from Cretaceous red beds evaporites, with a final addition of some seawater or shallow sediment fluids.

To verify the sources of ore-forming fluids, we used the binary plot between Sr and S isotope ratios (Fig. 10). Previous studies of Forghani-Tehrani (2003) and Rajabzadeh (2007) reported δ^{34}S values of +22.6 to +26.8 ‰ for epigenetic barites at Komsheche. These values are higher than those of the Middle Triassic (18.5-21.6‰, Nielsen and Ricke, 1964), higher than those of the Middle Eocene seawater (20-22‰, Claypool et al., 1980; Bottrell and Newton, 2006), and mostly, slightly higher than the Miocene seawater sulfate (22.75‰, Paytan et al., 1998). The high δ^{34}S values can be explained by sulfate leached from red beds evaporites or S from brine sulfate provided by seawater sulfate. However, the abnormally higher than coeval seawater may be explained by a Rayleigh-distillation process (cf. Canet et al., 2005). In contrast, Shafaezadeh (2012) obtained a wide range of δ^{34}S values (4.7 to 17.1‰; unpublished data) for barite from the Pinavand FBA mine (Fig. 2). These values can be compared to those of Schwarzwald FBA deposits in SW Germany (Schwinn et al., 2006; Staude et al., 2011), although part of this range is similar to the δ^{34}S values of sulfates precipitated from Triassic seawater (11-14‰, Claypool et al., 1980). In addition to extensive Triassic units in the southeastern Pinavand area near the Abbas-Abad basement fault, there are in small outcrops (Fig. 2) with Devonian dark carbonate and siltstone with pyrite concentrations and plant remains (Bahrami et al., 2015; Königshof et al., 2016). Lower S isotopic values than to those of Komsheche appear to be related to (or reinforcing) complete or fast oxidation of sulfides (e.g., Staude et al., 2011) in the Devonian (average δ^{34}S$_{\text{weathering}}$ ~ 6‰; Chen et al., 2013) and were then mixed with seawater sulfate that had higher δ^{34}S. Thus, different δ^{34}S values of Komsheche and Pinavand barites must be due to variations in the S isotope composition of the mineralizing fluids derived from multiple sources of sulphur of local country rocks. As can be seen, the plotted Sr and S isotopic analyses of Komsheche share similarities with defined diagenetic barites of Griffith and Paytan (2012) (Fig. 10) which epigenetically precipitated in the subsurface from porewater. They are compatible with the reported ranges for Asturias fluorite (±Ba, Pb±Zn) deposits in N Spain; the latter have a Sm-Nd age for fluorite of 185 Ma (Sánchez et al., 2010), although Symons et al. (2017) using paleomagnetic methods proposed an Early Cretaceous chemical remnant magnetization age of 115±3 Ma for mineralization. Similar isotopic ranges have also been reported from Zaghouan in NE Tunisia (Late Miocene age, Souissi et al., 2013) and Sichuan FBA deposits in China (fluorites formed at 104±11, 129.7 and 31.8 Ma, Sm-Nd isochron ages, Zou et al., 2017; Wang et al., 2013; Tian et al., 2014, respectively).

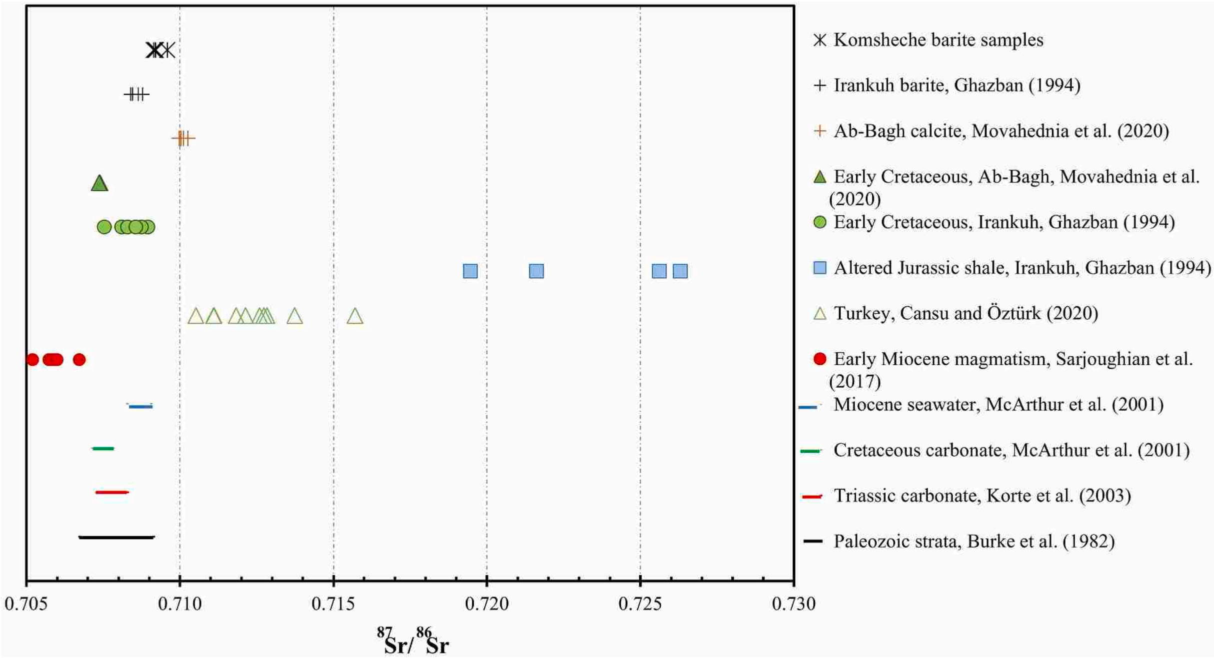

Fig. 9. Comparison of $^{87}Sr/^{86}Sr$ Komsheche barite samples with $^{87}Sr/^{86}Sr$ from Irankuh barite, sedimentary and magmatic rocks. Isotopic strontium compositions of: Paleozoic seawater (Burke et al., 1982), Triassic marine sediments (Korte et al., 2003), Cretaceous carbonate (McArthur et al., 2001), Irankuh barite and Ab-Bagh calcite with a Cretaceous age (Ghazban et al., 1994; Liu et al., 2019; Movahednia et al., 2020), Paleozoic sediment-hosted barite deposits of Turkey (Cansu and Öztürk, 2020), Miocene seawater (McArthur et al., 2001), and Isfahan Miocene granodiorite (Sarjoughian et al., 2017).

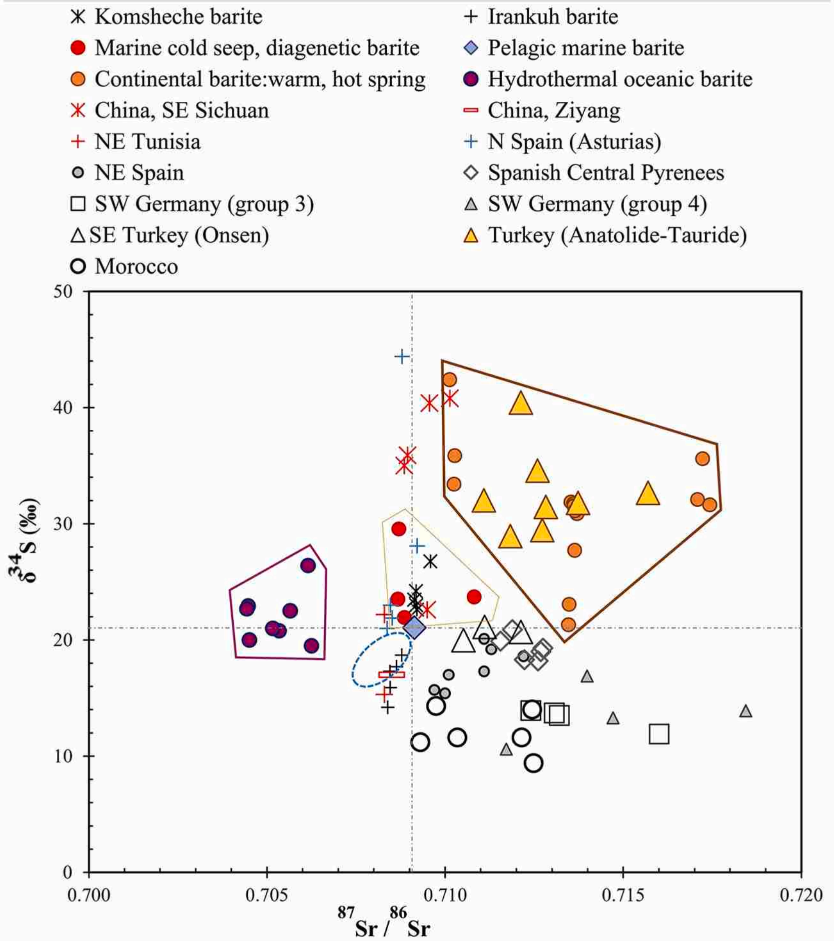

Fig. 10. Binary plot of $\delta^{34}S_{CDT}$ vs. Sr isotopic ratios for Komsheche barite samples (S isotopic data of Komsheche from Rajabzade, 2007 and Irankuh barite samples S and Sr isotopic data from Ghazban et al., 1994). All data of marine, hydrothermal, diagenetic, and cold seep barites are from Griffith et al. (2018). Dashed grey lines show the isotopic composition of modern seawater (blue diamond, Paytan et al., 1993). The blue oval shows the general evolution from Triassic to the present of Sr isotopic ratio vs. $\delta^{34}S$ from seawater sulfate. Published barite data from sedimentary rock-hosted fluorite deposits plotted include: NE Spain (Canals and Cardellach, 1993), Spanish Central Pyrenees (Fanlo et al., 1998), Morocco (Valenza et al., 2000), N Spain (Sánchez et al., 2010), SW Germany (Staude et al., 2011), Ziang and southeastern Sichuan in China (Maynard and Okita, 1991; Zou et al., 2017), and NE Tunisia (Souissi et al., 2013) described in Table 1. For detailed descriptions of the above barites, the reader is referred to the Table 1. Turkey (Anatolide-Tauride) data is from Paleozoic sediment-hosted barite deposits (Cansu and Öztürk, 2020).

Our barite Sr and S isotopic results suggest a mixture from multiple sources: for Sr mainly a Paleozoic reservoir, minor Mesozoic clastic sedimentary rocks, and seawater, and for S mainly Cretaceous red bed evaporites with seawater. On the one hand, the narrow range of Sr and S isotope compositions (Fig. 10) during deposition of barite implies uniform mixing and suggests that a Sr-rich fluid from hot brines was mixed in an open system with Sr-poor fluid derived from seawater. The homogeneity of the Sr isotope composition is also attributed to a higher degree of interfacing of fluids with host rock dolstones (carbonate-buffered). On the other hand, inhomogeneous fluid-mixing would be more consistent with changes in the reported temperatures for barite (119° and 323°C). This scenario is supported by the results of microthermometry by Rajabzadeh (2007), although the inference should be treated with extreme caution due to the fact that homogenization temperatures of soft minerals such as barite are prone to error (Ramboz and Charef, 1988; Kontak and Sangster, 1998).

6.3. *Evolution of barite-forming fluids and paleoreconstruction*

In Mesozoic sediments northeast of Isfahan, extensive FBA deposits occur in the western part of the two major regional deep-seated ZFS and Abbas-Abad faults (Fig. 2). Stratabound barite bodies are located mainly within the suitable layers of Mid Triassic or Early Cretaceous carbonate strata, while veins and breccia barite mineralization is mostly restricted to subsidiary faults associated with the major regional faults. Komsheche is a prominent example of both styles of baritization. In a previous study by Rajabzadeh (2007), the Komsheche deposit was suggested to be of hydrothermal origin, implying that ore-forming fluids were affected by heating and probably by chemical exchanges with post-Eocene intrusive bodies during downward migration. If this model is valid, the exploration for FBA deposits in this region should be focused near igneous rocks. Our field data indicate instead that most deposits were formed rather far from the magmatic successions of the UDMA, but close to the major fault zones (see Fig. 2). In this sedimentary basin, information on fluid composition, channelways, transport and precipitation mechanisms involved in the mineralized system are most important for the exploration.

In the Komsheche area, barite bands are distributed in yellow dolostone horizons in the Shotori Fm. of Middle Triassic age. The presence of numerouse barite layers (Fig. 4A-B) may suggest repeated precipitation over a longer period. Petrographic observations indicate a close association of barite with ferroan dolomite and siderite minerals. Blasco et al. (2017) demonstrated the possibility of generating and injecting CO_2, released from alteration of hydrocarbon or dissolution of carbonate minerals, to precipitate carbonate (dolomite and calcite) and sulphate in a carbonate-evaporitic thermal system. In such a system aluminosilicate phases of K-feldspar and albite are in equilibrium in the deep reservior. The suggestion is consistent with the existence of CO_2 and hydrocarbon in Komsheche fluid inclusions (Rajabzadeh, 2007). We can also infer that the oxygen fugacity for barite formation (at shallow levels) was high because of the presence of siderite and ferroan dolomite. Reduction of sulphate by organic matter in sediments is locally plausible, producing H_2S that reacted with the metals, causing sulfide precipitation (e.g., galena). Galena with barite (breccia-type) was deposited from a warm dense brine with higher concentrations of Ca^{2+}, Mg^{2+}, and Mn (Valentino and Stanzione, 2003), with pH values in range of 4.0- 5.5 (Sverjensky, 1984; Leach et al., 2010). This brine acquired its salinity by halite dissolution (Sánchez et al., 2009) present in evaporated seawater and/or from leaching (halite and gypsum) of Early Cretaceous evaporite.

Geochemically, the barites samples at Komsheche are characterized by low REE concentrations, strong positive Eu anomaly, slightly negative Ce anomaly, low Ce/La ratios (<0.5), and higher LREE/HREE ratios (Forghani-Tehrani, 2003). Our interpretation of published geochemical data suggests that barites might be comparable to those inferred for typical seawater and deep-sea barite (Guichard et al., 1979) at rifted continental margins (cf. south California, Hein et al., 2007). The association of Mn oxide with barite, indicates that the negative Ce anomaly (oxidation of Ce^{3+}) could reflect higher oxidizing conditions and higher pH (above 6.5) (Loges et al., 2012). In addition, the positive Eu anomaly suggests either (I) a response to reducing conditions in the sediments at temperatures above ~250°C, or (II) feldspar alteration of detrital rocks at a sediment-water interface (Möller et al., 1994; Bau and Dulski, 1995). In support of the latter concept, hydrothermal fluids from altered feldspars in siliciclastic sediments of the Nayband Fm. have a preference for Eu^{2+}. The S isotope data indicate that a single sulphur reservoir cannot account for the barite mineralization. The Sr source data establish that Ba was likely transported from deep source rocks, possibly derived from leaching feldspars within the Paleozoic sediments, and ascended along faults to reach the site of deposition, mixing with shallower level fluids. The mixing is also supported by the observed wall-rock silicification.

6.4. *Inferred conditions of fluorite - forming fluids*

Several grabens formed in the Cretaceous in northeast Isfahan during the opening of the Neo-Tethys ocean at the margin of Central Iran. This process was related to crustal thinning. During early diagenesis and associated dolomitization the former fluorine-rich fluids appear to have ascended from greater depth along extensional fault zones of grabens and discharged laterally through the dolomite horizons to form bedding replacements and irregularly distributed, but sparse fluorite and quartz. Möller et al. (1980) clearly show that the conditions of fluorite nucleation are more favourable within the calcareous sediments during diagenetic dolomitization because of an increase of Ca^{2+} and a decrease of Mg^{2+} ions in the pore solution, accompanied by a slight increase of the F^- ion concentration resulting from the decay of MgF^+ complexes. Previous studies by Barker et al. (2009) confirmed that fluid flow pathways, such as a fault zone with pulverised material, could rapidly buffer a fluid with the wall rock.

The REE in fluorite provide important information for determining the ore genesis and environmental changes (e.g., Möller et al., 1976; Gültekin et al., 2003; Schwinn and Markl, 2005; Trinkler et al., 2005; Souissi et al., 2013; Öztürk et al., 2019). However, in the Komsheche samples, it was not possible to isolate by handpicking the various fluorite types due to tight mingling boundaries (Fig. 6) and thus the interpretation of the fluorite bulk analyses should be taken with caution. Broadly, low $\sum$REE contents of the Komsheche fluorites are consistent with a hydrothermal or continental origin (Guichard et al., 1979). These low REE contents may be related to a slightly higher pH of the fluids (Sánchez et al., 2006), which indicates an interaction with Shotori dolostone. Hence, replacement texture and subsequent fluid-rock interaction, accompanied by intense dissolution of host rock, imply that the Shotori dolostone was the source of Ca^{2+} in fluorite (e.g., Banerjee, 2015). The subhorizontal REE pattern and a gradual decrease from La to Lu, slight LREE enrichment relative to HREE, associated with a weak negative Ce anomaly (Fig. 6B) could indicate a normal marine origin or a basinal brine derived from marine water (Fleet et al., 1976; Nozaki, 2001; Souissi et al., 2013; Freslon et al., 2014). Slight differences between the various LREE patterns could reflect some interaction between fluids and surrounding rocks during fluid migration to form secondary fluorites. Slight MREE enrichment (of fluorite samples type-I, Z-1, Z-3, and Z-7) likely reflects contamination by organic components under suboxic-anoxic conditions (Freslon et al., 2014). The MREE-enrichment is also evidence for natural waters and acidic leachates (Johannesson and Lyons, 1995). In the younger generations, the coexistence of fluorite with sulfide, and presence of hydrocarbon in fluid inclusion, illustrates a relatively reducing environment under mild acidic near-natural conditions (cf., Sallet et al., 2005; Trinkler et al., 2005). In some cases, negative Ce anomalies without Eu anomalies are common in seawaters and marine carbonates (Martin et al., 1976; Sánchez et al., 2010; Freslon et al., 2014). Europium anomalies depend on the chemical, redox, and temperature conditions of the hydrothermal solution (Castorina et al., 2008). Lack of positive or negative Eu anomaly can be dependent on temperatures lower than 200 °C or 250 °C, consistent with the former fluid inclusion studies (temperatures of 89° to 244°C) of Rajabzadeh (2007), or increasing oxygen fugacity and pH (Bau, 1991; Sánchez et al., 2009; Ehya, 2012; Deng et al., 2014). Positive Y anomalies point to a long migration pathway for the parent fluid (Jiang et al., 2005; Jian et al., 2015) with high stability Y-F complexes compared with Ho-F ligands (Bau, 1996). Several researchers noted a genetic relationship between the physico-chemical conditions for fluorite formation with Tb/Ca, Tb/La, La/Lu, Yb/La, Y/Ho, and La/Ho ratios. Forghani-Tehrani (2003) shows that Komsheche fluorite samples originate from a hydrothermal fluid based on a Tb/Ca (mean of 1.8×10^{-6}) versus Tb/La (mean of 0.36) ratios of Möller et al. (1976). The La/Lu ratios (22-178) of Komsheche are similar to those characterizing hydrothermal fluids, in contrast to seawater that has La/Lu <1 (Goldberg et al., 1963; De Baar et al., 1985). The La/Lu ratio >1 is also indicative of a low pH fluid with low complexation of hydroxo- or carbonate ligand species and/or halogens (Bau and Möller, 1992). In such conditions, the REE- adsorption could be prevailing over the REE-complexation in the parent fluid (Schwinn and Markl, 2005). In addition, Ce_n/Gd_n values of fluorites are below unity, showing REE fractionation in the ore-forming fluid. The ratios Y/Ho changed from 87 to 150, with a mean of 113, higher than the chondritic Y/Ho values (Anders and Grevesse, 1989), in accordance with Y-complexation, fluid-rock interaction and remobilization over a long migration distance (Schönenberger et al., 2008) and are comparable with hydrothermal fluorites (Bau and Dulski, 1995). It seems plausible that the primary fluorite could have been remobilized into veins and veinlets, and then deposited in dolostone, limestone and siliciclastic rocks. More interestingly, the REE pattern and low values of Nb+Ta (~1.43 ppm) of Komsheche fluorites have a similarity to the Turkey carbonate-hosted fluorites (e.g., Akkaya, Yeşilyurt, and Tavşanlı deposits). It is believed that they were formed in the Late Cretaceous to Miocene or even Pliocene (Fig. 11) and are situated close to the margin of the Alpine orogenic belt (Genç, 2006; Öztürk et al., 2019).

In addition, three likely sources of fluorine can be proposed. The first is from dissolution and leaching of minerals in coaly clastic Mesozoic sediments. The second are organic-rich metamorphic fluids, as Liu et al. (2015) suggested for the fluorite-rich MVT deposits of China related to the Alpine-Hymalayan orogeny. Tropper and Manning (2007) also reported increased fluorite dissolution and mobility will by saline brines in high P-T igneous and metamorphic environments. The third source are volcanogenic and fumarolic fluorides supplied to seawater basins by high heat flow and geothermal gradients in thinned continental crust.

Textural relationships preserved for barite and fluorite minerals, and a detailed comparison of their REE geochemistry and fluid inclusion types reveal that different generations did not grow contemporaneously. Thus, the minerals did not form from a single parent fluid with a uniform composition.

6.5. *Genetic model for Komsheche FBA deposit*

The conclusions of the previous paragraphs indicate that we are dealing with poly-phase deformation and in turn, multiple reactivations and reworking of the fault damage zones at Komsheche under the variable regional stress regimes (ranging from extensional to compressional) since Cretaceous time. The age and formation mechanism of FBA deposits in northeast Isfahan provide important guides for future exploration. Fault damage zones, i.e. weak zones in the crust with rather high permeability, are most favorable for circulation of meteoritic and hydrothermal fluids among the impermeable rock units (Wiprut and Zoback, 2000; Faulkner et al., 2010; Rossetti et al., 2011). The studies of Cathles (2007, 2019) reveal that mineralization of MVT deposits occurred during multiple episodes (Fig. 11) lasting short periods of time (<200 ky) due to multiple pulses of brine expulsion, which suddenly released gas to the brine-filled aquifers in sedimentary basins.

As discussed above, all results presented in this research including mineralogy, geochemistry, thermochronology, isotopic, and tectonic evidences propose that the Komsheche mineralized levels formed during two distinct episodes as follows.

The first episode corresponds to the extensional regime in the Early Cretaceous. At Komsheche, bands of colorless irregular crystals of fluorite-I associated with fine-grained quartz are well encased and fitted by Triassic dolomitic rocks. According to the (U-Th)/He age of fluorite formation measured at ~ 120 and 137 Ma (Aptian and Valanginian), paleographic reconstructions point to an extensional tectonic environment at a continental margin in northeast Isfahan. The large-scale extensional basement faults, such as the Abbas-Abad deep fault, provided fluid pathways. An increasing geothermal gradient, caused by crustal thinning, acted as a heating source for the circulation of basinal brines at depth along the fault. Subsequently, an extension regime contributed to release fluids towards shallower depths. Our studies show that the deposition of fluorite-I is attributed to a dilute hydrothermal fluid that resulted from mixing between an ascending heated fluid, leached sediment basement, and cool seawater/dolomite or surficial

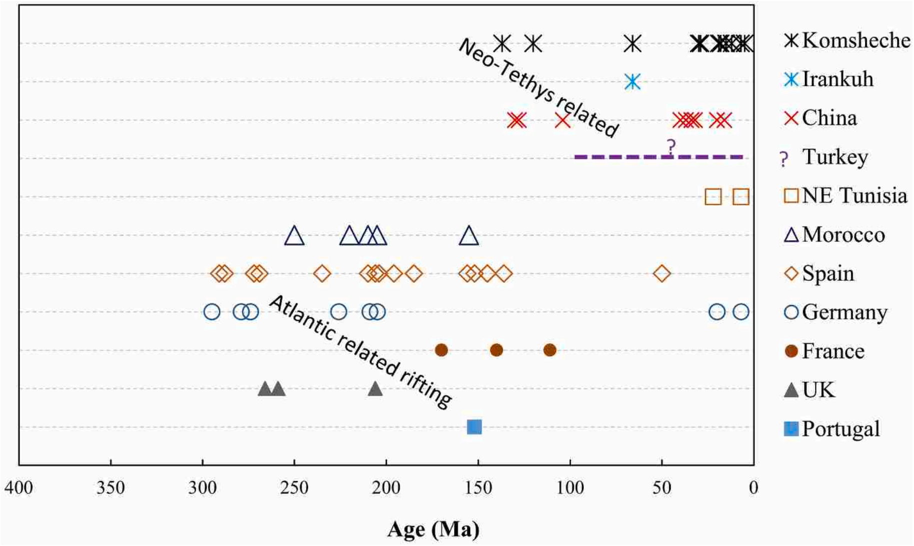

Fig. 11. Ages of sediment-hosted fluorine-bearing (±Ba, Pb±Zn) deposits in Asia and Europe (data sources from Table 1), including the Komsheche deposit (this work). All data on fluorite, with the exception of Irankuh, which is based on a Re-Os age of pyrite.

water dissolving red bed evaporites after a long migration in an anoxic to suboxic environment. The existence of hydrocarbon–bearing inclusions observed in the fluorite by the microthermometry of Rajabzadeh (2007), confirms weakly reducing conditions during the transportation. Precipitation of fluorite-I is thought to have occurred due to enrichment of calcium by the dissolution of Triassic dolostone while fluorine in this fluid was possibly sourced from the submarine volcanic gases or from low grade to non-metamorphic sedimentary successions of mainly Triassic siliciclastic composition. Banded barite replacements associated with ferroan dolomite could be related to a late-diagenetic condition that resulted from the mixing of sulfur- and barium-rich fluids (Ba and S gained from altered clastic strata and red bed evaporites, respectively) with seawater at an oxic-anoxic interface. There is a fairly good agreement on the Mesozoic crustal extension scenario linking the Komsheche FBA deposit to the Neo-Tethys opening, and the FBA deposits to the Atlantic opening. The latter is reflected, for example, in the deposits of Morocco (Margoum et al., 2015), Spain (Tornos et al., 2000; Sánchez et al., 2010), Germany (Lüders and Möller, 1992; Schwinn and Markl, 2005), France (Munoz et al., 2005), and UK (Kraemer et al., 2019) (Fig. 11; and Table 1).

The second episode corresponds to the compressional regime after the Early Cretaceous. The presence of an active fluid phase within the fault zone of the Komsheche deposit is indicated by FBA mineralized breccias and veins in the fault gouge (Fig. 5B and C). The deposition of later FBA generations (or several FBA mineralizing events), occurred within a varied time frame (5-66 Ma), during the transition from extensional to compressional tectonism of hinterland basin sediments. Compressional tectonism could be characterized by the presence of a folded and banded FBA-bearing Triassic unit (the fold formed after stage-I of FBA). The compression-related thrusting at Komsheche provided favorable lithological and structural traps for basinal brines by shortening and thickening of strata. In this respect, the content of ions (e.g., Mg^{2+}, Ca^{2+}, and F) in trapped fluids increased due to dissolution of dolostone and exchange reactions of brines with different rock types. A tectonic pumping mechanism could have been cyclically changing the fluid composition from different reservoirs (Sibson et al., 1975). Thus, fault movements over a long period mixed and diluted trapped fluids by external waters (e.g., seawater) until active strike-slip faulting opened favorable corridors promoting the ascent of ore-forming fluid flows or partial remobilization from different crustal levels (or release towards) to shallower depth and diffusion into the immediate hangingwall of the fault zones (Fig. 5A- C). The Sr isotope composition reflects mixing and dilution of the hydrothermal fluid at the site of barite deposition. The compression-related FBA formation hypothesis is supported by the occurrence of FBA deposits in northern Tunisia (Jemmali et al., 2011), northeastern Tunisia (Souissi et al., 2013), southwestern Germany (Staude et al., 2011), Spain (Symons et al., 2017), Turkey (Öztürk et al., 2019), and China (Liu et al., 2015), all along the Alpine-Himalayan orogen (Figs. 1A and 11).

According to the field data, and isotopic and dating results, we can conclude that the contemporaneous and mutual interaction between fault damage zones as a corridor and FBA contaminated fluid flow (which carried the fluids to carbonates located adjacent to the fault damaged zones) facilitated the deposition of FBA occurrences in the study area (Fig. 12A, B).

6.6. Rationale linkage between Komsheche FBA mineralization and regional tectonic evolution

The direct connection between tectonics and magmatism (Pearce et al., 1984; Pearce and Stern, 2006; Wright et al., 2016) has been studied for years, as well as the coupling between tectonic setting and mineralization (i.e., Kyser, 2007; Richards and Sholeh, 2016). With this idea in mind, and taking into account that the study area is located in the hinterland of the Zagros convergent zone, we attempt to correlate our Komsheche tectonic, stratigraphic, geochronological, and isotopic data with the published data for the region and at the scale of the overriding plate of the Zagros collision zone. The results are a compiled in a schematic tectonostratigraphic chart of the region since the Early Cretaceous accompanied by regional tectonic events (Fig. 13).

The evolution starts when the region experienced enhanced extension during the Early Cretaceous extensional phase of the Neo-Tethys.

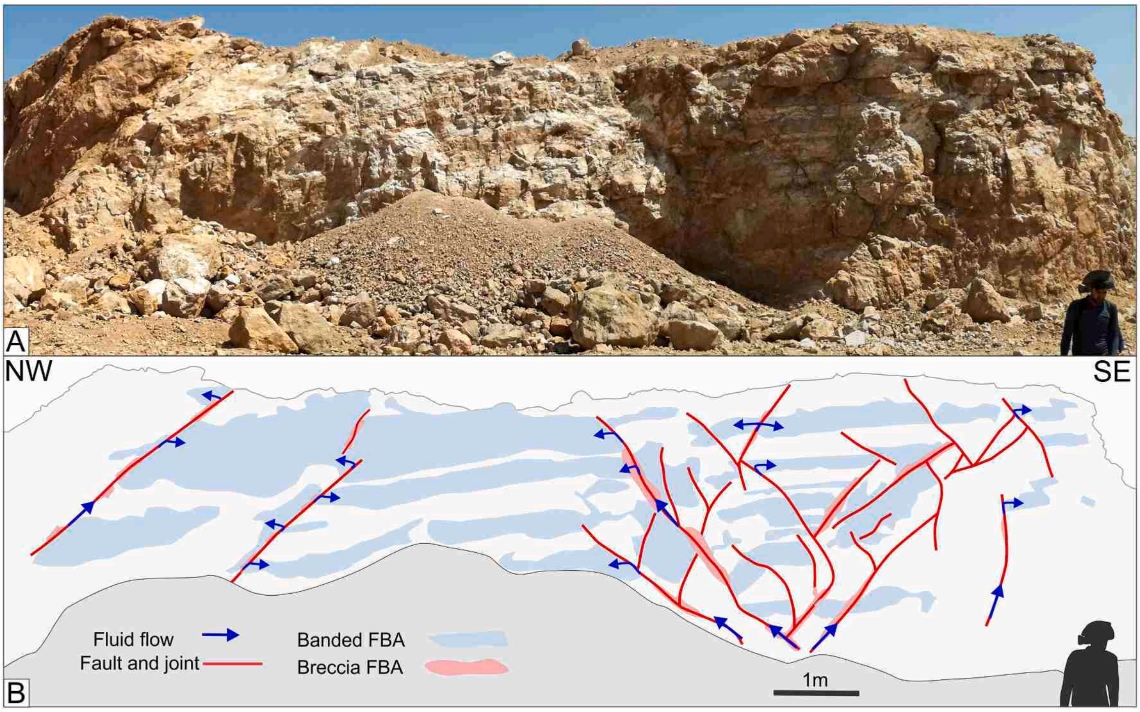

Fig. 12. (A) Panoramic view showing the FBA-bearing Shotori Fm. that is intensively cut by fault strands. (B) Line-drawing of Fig. 12A illustrates schematically the formation of the carbonate hosted FBA mineralization by interaction of fault damage zone and fluid flow.

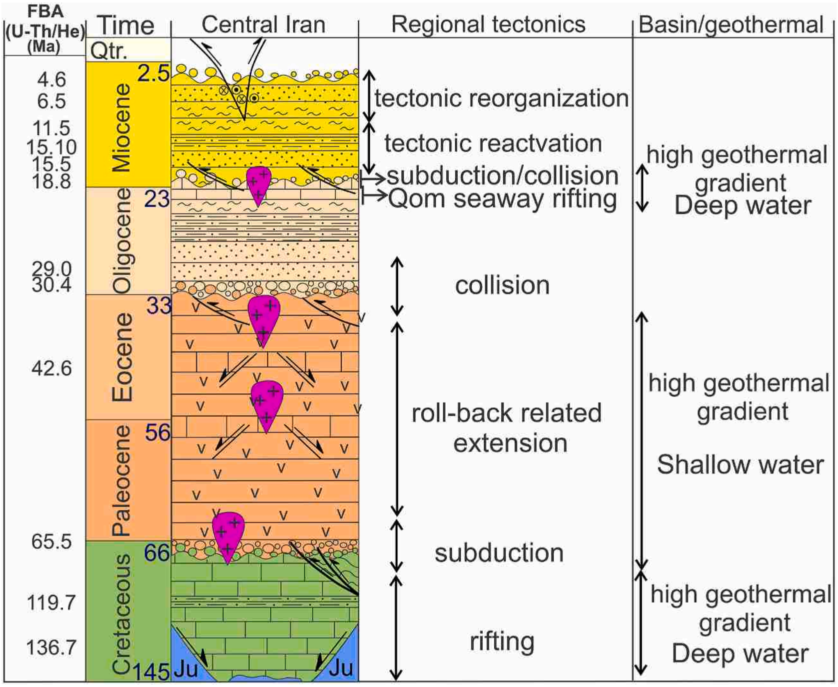

Fig. 13. Post Jurassic tectonostratigraphic chart of the western edge of Central Iran. Chart is adapted and modified after Radfar et al. (1999), Safaei et al. (2008), Allen and Armstrong (2008), Barrier et al. (2008), Mannani and Yazdi (2009), Verdel et al. (2011), McQuarrie and van Hinsbergen (2013), Francois et al. (2014), Wilmsen et al. (2015), Tabaei et al. (2016), Tadayon et al. (2017, 2019), Salehi et al. (2018), and Alaminia et al. (2020).

This phase was associated with a high geothermal gradient (Berberian and King, 1981; Barrier et al., 2008; Wilmsen et al., 2015). Around Komsheche the extension was accommodated along the NW-SE ZFS and N-S Abbas-Abad faults (Fig. 2; Radfar et al., 1999; Safaei et al., 2008; Tabaei et al., 2016) and caused a progressive deepening of the depositional level of the Cretaceous strata, which overlie unconformably the Shemshak Fm. (Radfar et al., 1999; Mannani and Yazdi, 2009). These events were followed by the Late Cretaceous-Paleocene subduction of the Neo-Tethys oceanic slab underneath Central Iran (Berberian and King, 1981; Agard et al., 2007). The region was subjected to a NE-SW-directed compression regime and uplifted, which resulted in the deposition of conglomerate and sandstone (Radfar et al., 1999; Tadayon et al., 2019; this study). Thereafter it was affected by the Paleogene magmatic flare-up accompanied by an increase of the geothermal gradient (Berberian and Berberian, 1981; Verdel et al., 2011), and then by Neo-Tethys slab roll back-related extension, which further increased the geothermal gradient (Verdel et al., 2011; Tadayon et al., 2019). These Paleogene events were associated to the deposition of a thick pile of volcaniclastics and limestone strata (Radfar et al., 1999).

Late Eocene-Earliest Oligocene times correspond to the advance of the Zagros trench and hence initiation of the collision between the Arabian and Iranian plates and regional uplift (Allen and Armstrong, 2008; McQuarrie and van Hinsbergen, 2013; Francois et al., 2014; Tadayon et al., 2017). It resulted in the deposition of Oligocene detrital red beds, overlain by a layer of marls, which is called Lower Red Bed Fm. (Radfar et al., 1999; Tadayon et al., 2019).

In the Late Oligocene - Early Miocene a regional extensional regime caused crustal thinning and resulted in the formation of the Qom Seaway with deposition of carbonate of the Qom Fm. (Reuter et al., 2007; Morley et al., 2009; Amirshahkarami and Karavan, 2015) and in turn it increased the geothermal gradient of the region. Consequent renewed compression and uplift due to subduction of the Qom seaway affected the region. It was associated with extensive Latest Oligocene to Earliest Miocene magmatism forming the UDMA (Radfar et al., 1999; Berberian and Berberian, 1981; Francois et al., 2014; Sarjoughian and Kananian, 2017; Babazadeh et al., 2017; Alaminia et al., 2020), which also increased the geothermal gradient of the region. This was followed by a Middle-Late Miocene tectonic reorganization in the Arabia-Eurasia collision zone (McQuarrie and van Hinsbergen, 2013; Tadayon et al., 2017, 2019; Salehi and Tadayon, 2020). This regime emerged in the form of an accommodation of E-W fold axes, overprinting on NW-SE trending folds, and reactivation of the ZFS and Abbas-Abad faults with right-lateral and transtensional kinematics in the study area, respectively (Safaei et al., 2008; Alaminia et al., 2020). This event corresponds to extensive hydrothermal activity coupled with tectonism that resulted in the deposition of widespread travertines along the main fault zones (Radfar et al., 1999; Taghipour et al., 2010; Dehbozorgi and Momeni, 2016) (Fig. 2).

Comparison of the (U-Th)/He geochronological results with the tectonostratigraphic column in Fig. 13 suggests that: 1) FBA mineralization was episodic, and 2) interestingly, FBA mineralization occurred synchronously with events / periods of tectonic activity, both in compressional and extensional regimes (Fig. 13). The data are thus in good agreement with the published thermochronology in the region (Francois et al., 2014) and in the far-field hinterland zone (Karganbafghi et al., 2012; Francois et al., 2014; Calzolari et al., 2016; Tadayon et al., 2017, 2019). They reflect the direct impact on the mineralization of the FBA of the tectonic activity in the study area controlled by the punctuated Zagros orogenic evolution (Agard et al., 2011). Furthermore, it can be inferred that tectonic activity provided optimal conditions for FBA mineralization, such as increased geothermal gradients by thinning the crust during extension and/or magmatism, and hydrothermal connectivity from depth to surface via the basement fault zones. The latter are crustal weak zones that enable transmission and circulation of fluids in the crust (Wiprut and Zoback, 2000; Faulkner et al., 2010; Rossetti et al., 2011).

Collectively, two crucial points can be inferred: 1) identifying episodes of tectonic activity in a region is an essential key for the exploration of FBA mineralization, and 2) the (U-Th)/He geochronology, with such a low closure temperature window, is a reliable chronometer for dating and detecting the fault/tectonic activities (e.g., Pi et al., 2005; Wolff et al., 2015, 2016). Integration of the tectonostratigraphic and geochronological data of the region implies that the ZFS and Abas-Abad fault zones (major intraplate deformation zones in the hinterland of the Zagros orogen) together and in synchrony accommodated the stresses transferred from the Zagros convergent margin during the prolonged Arabia-Eurasia convergence since Cretaceous time.

6.7. *Sediment-hosted FBA deposits of Iran and other areas*

The central segment of the boundary zone of Central Iran with other structural zones contains the economically most important sediment-hosted FBA deposits, including four clusters within metallogenic belts at Malayer-Isfahan, central Alborz, Yazd-Anarak, and Poshte-badam (Fig. 1B). The comparison of the results from this study with those of other areas (Table 1) indicates the following first-order similarities in geological environment and fluid composition for FBA deposits: (1) Besides the existence of a host rock with sufficient porosity (predominatly Triassic in age), they are associated with clastic units containing organic and evaporite matter situated below the host rock (i.e., Cathles, 2019). (2) They are strictly structurally controlled, usually formed in an extensional environment around reactivated steeply-dipping faults (i.e., Souissi et al., 2013; Symons et al., 2017). The faults allow the expulsion of ascending deep-seated ore-forming fluids driven by the production of a geothermal gradient. (3) There is not necessarily a relationship with magmatic activity. (4) Dolomitization and silicification are the most common types of alteration in wall rocks, although argillization and chloritization are also reported in several deposits (Table 1). (5) FBA mineralization occurs epigenetically as veins, stratabound, and in breccia with simple mineral assemblages. (6) Mixing between distinct fluids enriched in Ba and SO_4, and interaction of ascending fluorine-rich fluids with Ca-rich fluids derived from dolostone, respectively, are the dominant process in barite and fluorite precipitation (e.g., Hanor, 2000; Griffith and Paytan, 2012; Liu et al., 2015; Symons et al., 2017; Graaf et al., 2019; Kraemer et al., 2019). Salinity values in fluid inclusions of reported FBA deposits are in the range from 0.5 to 34 wt% NaCl equivalent, with the majority falling between 10 and 30 wt% NaCl equivalent, and homogenization temperatures range between 90 and 390 °C, with the majority falling between 90 and 210 °C (Table 1).

There are two meaningful indicators (S and Sr isotopes) of barite ore control corresponding to regional-scale variations in tectonic activities. They reflect extensional processes, one type leading to the formation of continental margins and the others to rifting. Exceptions are Tunisia and Spain in Figure 10 indicating different processes of mineralization. Whereas evaporites dissolution and/or seawater are assumed to be the sources of sulphate, barite samples of rift-related deposits show distinctive, lower values of $\delta^{34}S$ (+9 to +21‰, see Table 1) than the continental margin related clan. Because of the high temperature of ore-forming fluid in FBA, bacterial processes (bacteriogenic activity occurs below 110 °C; Jørgensen et al., 1992) are rarely a factor in the formation of these deposits (Sánchez et al., 2010). The strontium isotopic composition of barite in FBA deposits (Fig. 10) can be grouped into 1) $^{87}Sr/^{86}Sr > \sim 0.709$, and 2) $^{87}Sr/^{86}Sr = 0.708$ to 0.710. The deposits of the first clan have a common dynamic evolution related to rifting during opening of the Atlantic. The time of FBA mineralization of this group ranges from the Early Permian (291 Ma, ~Sakmarian) to Early Cretaceous (111 Ma, ~Aptian; Sm-Nd ages of fluorite). In the second group, China and Iran's FBA deposits fall within the range of continental margin, in relation to the development of the Alpine-Himalayan orogen. The mineralizing event in China occurred between the Early Cretaceous (130 Ma, ~Barremian) and the Middle Miocene (16 Ma, ~Burdigalian). In the continental margin-related group, the metallogenic ages of fluorite are consistent with age data at Komsheche. Some authors also propose that remobilization of deep-seated primary deposits is very probable for the origin of several FBA veins. For instance, formation of some FBA deposits of NE Tunisia and SW Germany occurred in the Miocene by the reactivation during the Alpine orogeny (Staude et al., 2011; Souissi et al., 2013).

7. Conclusions

In this study we have discussed on the sources and possible pathways of ore-forming fluid-flow, structures, and the timing of the carbonate-hosted FBA deposits. We focus on the Komsheche deposit, where the relationships between mineralization and tectonics in the Central Iran have been of considerable debate for the last two decades. The Komsheche FBA deposit displays a variety of features similar to those which are typical of epigenetic FBA mineralisations in sedimentary rocks (Table 1). These features are the following:

1. The Komsheche FBA mineralization occurs as stratabound, cavity- and vein- filling, and breccia cementation along the fault-boundary between Middle Triassic host dolomite with Late Triassic siliciclastic rocks and Early Cretaceous limestone.
2. The anatomy of the Komsheche deposit has been affected by a multiphase tectonic history. In the Cretaceous, during the formation of the Neo-Tethys, NW-SE striking extensional faults cut through Triassic carbonates. In the Paleocene these structures were inverted to form reverse faults and folds in response to Neo-Tethys subduction. In the Neogene they became right-lateral faults during the Zagros collision.
3. The radiogenic Sr isotope ratios of the older barite generation reveal that the mineralizing fluid was linked to basinal (connate) brines, which were derived from more deeply buried sedimentary strata of a Paleozoic reservoir, while the Sr isotope composition of the younger barite generation is closest to that of Miocene seawater. The homogeneity in the Pb isotope compositions of galena points to leaching of the lead from a single upper crustal source.
4. At the Komsheche deposit, the REE behaviour of the fluorite types could be traced from a normal marine origin or a basinal brine, older samples (of fluorite type-I, Z-1, Z-3, and Z-7) show a relatively reducing environment under mild acidic near-neutral conditions of deposition.
5. The (U-Th)/He thermochronology of some Komsheche fluorite varieties constrain several depositional periods: Cretaceous (136.7 to 65.5 Ma) and Eocene to Miocene (42.6 to 4.6 Ma) (Fig. 13).
6. Based on our new results, we suggest a mixing model during fluid migration along aquifers to the sites of FBA. Hence we propose that fluorite and barite deposition took place in two-stage pattern as follows:

i) The Early Cretaceous and Oligocene-Miocene opening of the Neo-Tethys affected the western margin of the Central Iran zone, establishing a local extensional environment, northeast of Isfahan. The process was associated with the onset of thinning of the continental crust and hot fluids were generated by the geothermal gradient at depth bringing up F and Ba released during diagenesis. Fluorite precipitated when hot F-bearing brines mixed with descending oxygenated seawater and interacted with the host dolostone during dolomitization. Banded-type barite precipitated when Ba-bearing hydrothermal fluids ascending from depth encountered sulfate-bearing marine waters.

ii) The post-Cretaceous to Oligocene closure of the Neo-Tethys Ocean and Miocene onward collision generated a tectonic pumping mechanism allowing the mixing and further interaction of compositionally diverse fluids with the Triassic dolostone-host rock. The deposition of vein and breccia FBA is proposed to result from the mixing and increase in pH of the mineralizing fluid resulting in the precipitation of the ore into structural traps.

7. Spatial-temporal correlation of the current study's results with those along the Alpine-Himalayan and Atlas Mountains domain reveal a tight linkage between tectonic activities and formation of sediment-hosted fluorine-bearing (±Ba, Pb±Zn) deposits through Mesozoic-Cenozoic times. The first deposits formed during the initiation of Mesozoic extensional-related basement faults and the new

generations of deposits were synchronous with the late Mesozoic-Cenozoic reactivation of pre-existing structures.

Declaration of Competing Interest

The authors declare that they have no known competing financial interests or personal relationships that could have appeared to influence the work reported in this paper.

Acknowledgments

This research was supported by the University of Isfahan. Thanks go to K. Heydarpour, N. Tayebi, and E. Babamir for their assistant during field works. We would deeply appreciate kind hospitality of Iran Barite Falat Co. during field work at the Komsheche mine. Prof. David Lentz and an anonymous reviewer, as well as Editor-in Chief Dr. Böttcher are gratefully acknowledged for their constructive comments, which greatly helped to improve the manuscript.

References

Agard, P., Omrani, J., Jolivet, L., Mouthereau, F., 2005. Convergence history across Zagros (Iran): constraints from collisional and earlier deformation. Int. J. Earth Sci. 94, 401–419.

Agard, P., Jolivet, L., Vrielynck, B., Burov, E., Monie, P., 2007. Plate acceleration: the obduction trigger? Earth Planet. Sci. Lett. 258, 428–441.

Agard, P., Omrani, J., Jolivet, L., Whitechurch, H., Vrielynck, B., Spakman, W., Monié, P., Meyer, B., Wortel, R., 2011. Zagros orogeny: a subduction-dominated process. Geol. Mag. 148, 692–725.

Aghanabati, A., 1998. Major sedimentary and structural units of Iran (map). Scientific Q. J. Geosci. 7, 29–30.

Aghanabati, S.A., 2004. Geology of Iran. Geological Survey of Iran, Tehran (in Persian).

Alaminia, Z., Sharifi, M., 2018. Geological, geochemical and fluid inclusion studies on the evolution of barite mineralization in the Badroud area of Iran. Ore Geol. Rev. 92, 613–626.

Alaminia, Z., Salehi, M., Finger, F., 2017. Discovery of the Hendou-abad copper mineral district and its association to dikes: A reconstruction scenario for exploration of Cu-porphyry, northeast Isfahan. Iran. J. Geochem. Explor. 183, 88–101.

Alaminia, Z., Tadayon, M., Finger, F., Lentz, D.L., Waitzinger, M., 2020. Analysis of the infiltrative metasomatic relationships controlling skarn mineralization at the Abbas-Abad Fe-Cu deposit, Isfahan, north Zefreh Fault, Central Iran. Ore Geol. Rev. 117 https://doi.org/10.1016/j.oregeorev.2020.103321.

Alipour, S., Abedini, A., Talaie, B., 2015. Geochemical characteristics of the Qahr-Abad fluorite deposit, southeast of Saqqez, western Iran. Arab. J. Geosci. 8, 7309–7320.

Alirezaei, S., 1985. An investigation in stratigraphy and genesis of F-Pb-Ba deposits in the Central Alborz. M.S. thesis. Tehran University, Iran (in Persian).

Allen, M.B., Armstrong, H., 2008. Arabia-Eurasia collision and the forcing of mid-Cenozoic global cooling. Palaeogeogr. Palaeocl. 265, 52–58.

Allen, M., Jackson, J., Walker, R., 2004. Late Cenozoic reorganization of the Arabia-Eurasia collision and the comparison of short-term and long-term deformation rates. Tectonics 23. https://doi.org/10.1029/2003TC001530.

Ameri, H., Yazdi, M., Bahrami, A., 2017. Pseudophillipsia (Carniphillipsia) (Trilobite) from the Permian Jamal Formation, Isfahan, Iran. J. Sci. Islamic Republic of Iran 28 (4), 325–336.

Amirshahkarami, M., Karavan, M., 2015. Microfacies models and sequence stratigraphic architecture of the Oligocene-Miocene Qom Formation, south of Qom City, Iran. Geosci. Front. 6, 593–604.

Anders, E., Grevesse, N., 1989. Abundances of the elements: meteoric and solar. Geochim. Cosmochim. Acta 53, 197–214.

Arvin, M., Pan, Y., Dargahi, S., Malekizadeh, A., Babaei, A., 2007. Petrochemistry of the Siah-Kouh granitoid stock southwest of Kerman, Iran: Implications for initiation of Neotethys subduction. J. Asian Earth Sci. 30, 474–489.

Austermann, J., Iaffaldano, G., 2013. The role of the Zagros orogeny in slowing down Arabia-Eurasia convergence since ~5 Ma. Tectonic 32, 351–363.

Babazadeh, S., Ghorbani, M.R., Bröcker, M., D`Antonio, M., Cottle, J., Gebbing, T., Carmine Mazzeo, F., Ahmadi, P., 2017. Late Oligocene–Miocene mantle upwelling and interaction inferred from mantle signatures in gabbroic to granitic rocks from the Urumieh–Dokhtar arc, south Ardestan. Iran. Int. Geol. Rev. 59, 1590–1608.

Bahrami, A., Königshof, P., Boncheva, I., Tabatabaei, M.S., Yazdi, M., Safari, Z., 2015. Middle Devonian (Givetian) conodonts from the northern margin of Gondwana (Soh and Natanz regions, north-west Isfahan, Central Iran): biostratigraphy and palaeoenvironmental implications. Palaeobio. Palaeoenv. 95 (4), 555–577.

Banerjee, A., 2015. Groundwater fluoride contamination: A reappraisal. Geosci. Front. 6, 277–284.

Barker, S.L., Bennett, V.C., Cox, S.F., Norman, M.D., Gagan, M.K., 2009. Sm–Nd, Sr, C and O isotope systematics in hydrothermal calcite–fluorite veins: implications for fluid–rock reaction and geochronology. Chem. Geol. 268 (1-2), 58–66.

Barrier, E., Vrielynck, B., Bergerat, F., Brunet, M.F., Mosar, J., Poisson, A., Sosson, M., 2008. Palaeotectonic maps of the Middle East: Tectono-sedimentary-Palinspastic maps from Late Norian to Pliocene. In: Atlas of 14 maps at 1/18,500,000. CGMW, Paris, France.

Bau, M., 1991. Rare earth element mobility during hydrothermal and metamorphic fluid rock interaction and the significance of the oxidation-state of europium. Chem. Geol. 93, 219–230.

Bau, M., 1996. Controls on the fractionation of isovalent trace elements in magmatic and aqueous systems: evidence from Y/Ho, Zr/Hf, and lanthanide tetrad effect. Contrib. Miner. Pet. 123, 323–333.

Bau, M., Dulski, P., 1995. Comparative study of yttrium and rare earth element behaviors in fluorine-rich hydrothermal fluids. Contrib. Miner. Pet. 119, 213–223.

Bau, M., Möller, P., 1992. Rare earth element fractionation in metamorphogenic hydrothermal calcite, magnesite and siderite. Miner. Pet. 45, 231–246.

Bellanca, A., De Vivo, B., Lattanzi, P., Maiorani, A., Neri, R., 1987. Fluid inclusions in fluorite mineralizations of northwestern Sicily, Italy. Chem. Geol. 61 (1-4), 209–216.

Berberian, F., Berberian, M., 1981. Tectono-plutonic episodes in Iran. Zagros Hindu Kush Himalaya Geodynamic Evolution 3, 5–32.

Berberian, M., King, G.C.P., 1981. Towards a paleogeography and tectonic evolution of Iran: Can. J. Earth Sci. 18, 210–265.

Beygi, S., Nadimi, A., Safaei, H., 2016. Tectonic history of seismogenic fault structures in Central Iran. J. Geosci. 61, 127–144.

Blasco, M., Auqué, L.F., Gimeno, M.J., Acero, P., Asta, M.P., 2017. Geochemistry, geothermometry and influence of the concentration of mobile elements in the chemical characteristics of carbonate-evaporitic thermal systems. The case of the Tiermas geothermal system (Spain). Chem. Geol. 466, 696–709.

Bottrell, S.H., Newton, R.J., 2006. Reconstruction of changes in global sulfur cycling from marine sulfate isotopes. Earth Sci. Rev. 75, 59–83.

Boveiri Konari, M., Rastad, E., 2017. Nature and origin of dolomitization associated with sulphide mineralization: new insights from the Tappehsorkh Zn-Pb (-Ag-Ba) deposit, Irankuh Mining District, Iran. Geol. J. 53, 1–211.

Boveiri Konari, M., Rastad, E., Mohajjel, M., Nakini, A., Haghdoost, M., 2016. Structure, texture, mineralogy and genesis of sulphide ore facies in Tappehsorkh detrital-carbonate-hosted Zn-Pb-(Ag) deposit, south of Esfahan. Sci. Q. J. Geosci. 25, 221–236 (in Persian with English abstract).

Burke, W.H., Denison, R.E., Hetherington, E.A., Koepnick, R.B., Nelson, H.F., Otto, J.B., 1982. Variation of seawater ^{87}Sr/^{86}Sr throughout Phanerozoic time. Geology 10, 516–519.

Burnol, L., 1968. Contribution a l'etude des gisements de plomb et zinc de l'Iran. Essais de classification paragenetique. Geol. Survey Iran Rep. (11).

Calzolari, G., Rossetti, F., Della Seta, M., Nozaem, R., Olivetti, V., Balestrieri, M.L., Vignaroli, G., 2016. Spatio-temporal evolution of intraplate strike-slip faulting: The Neogene–Quaternary Kuh-e-Faghan Fault, central Iran. GSA Bulletin 128, 374–396.

Canals, A., Cardellach, E., 1993. Strontium and sulphur isotope geochemistry of low-temperature barite-fluorite veins of the Catalonian Coastal Ranges (NE Spain): a fluid mixing model and age constraints. Chem. Geol. 194, 269–280.

Canet, C., Alfonso, P., Melgarejo, J.C., Fallick, A.E., 2005. Stable isotope geochemistry of the Carboniferous Zn-Pb-Cu sediment-hosted sulfide deposits, northeastern Spain. Int. Geol. Rev. 47, 1298–1315.

Cansu, Z., Öztürk, H., 2020. Formation and genesis of Paleozoic sediment-hosted barite deposits in Turkey. Ore Geol. Rev. 125, 103700.

Castorina, F., Masi, U., Padalino, G., Palomba, M., 2008. Trace-element and Sr–Nd isotopic evidence for the origin of the Sardinian fluorite mineralization (Italy). Appl. Geochem 23, 2906–2921.

Cathles, L.M., 2007. Changes in sub-water table fluid flow at the end of the Proterozoic and its implications for gas pulsars and MVT lead–zinc deposits. Geofluids 7, 209–226.

Cathles, L., 2019. On the Processes that Produce Hydrocarbon and Mineral Resources in Sedimentary Basins. Geosci. 9, 520.

Chen, D., Wang, J., Racki, G., Li, H., Wang, C., Ma, X., Whalen, M.T., 2013. Large sulphur isotopic perturbations and oceanic changes during the Frasnian–Famennian transition of the Late Devonian. J. Geol. Soc. London 170 (3), 465–476.

Chiu, H.Y., Chung, S.L., Zarrinkoub, M.H., Mohammadi, S.S., Khatib, M.M., Iizuka, Y., 2013. Zircon U-Pb age constraints from Iran on the magmatic evolution related to Neotethyan subduction and Zagros orogeny. Lithos 162-163, 70–87.

Claypool, G.E., Holser, W.T., Kaplan, I.R., Sakai, H., Zak, I., 1980. The age curves of sulfur and oxygen isotopes in marine sulfate and their mutual interpretation. Chem. Geol. 28, 199–260.

De Baar, J.W., Bacon, M.P., Brewer, P., 1985. Rare earth elements in the pacific and Atlantic Oceans. Geochim. Cosmochim. Acta 49, 1943–1959.

de Lamotte, D.F., Leturmy, P., Missenard, Y., Khomsi, S., Ruiz, G., Saddiqi, O., Guillocheau, F., Michard, A., 2009. Mesozoic and Cenozoic vertical movements in the Atlas system (Algeria, Morocco, Tunisia): an overview. Tectonophysics 475, 9–28.

Dehbozorgi, M., Momeni, T.M., 2016. Recent tectonic activity in Qom-Zefreh fault zone, Central Iran. Quant. Geomorphological Res. 5, 110–129.

Deng, H.H., Chen, Y.J., Yao, J.M., Bagas, L., Tang, H.S., 2014. Fluorite REE-Y (REY) geochemistry of the ca. 850 Ma Tumen molybdenite–fluorite deposit, eastern Qinling, China: Constraints on ore genesis. Ore Geol. Rev. 63, 532–543.

Dill, H.G., Weber, B., Eigler, G., Kaufhold, S., 2012. The fluorite deposits NE of Regensburg, SE Germany-A mineralogical and chemical comparison of unconformity-related fluorite vein-type deposits. Geochemistry 72 (3), 261–278.

Ehya, F., 2011. Variation of mineralizing fluids and fractionation of REE during the emplacement of the vein-type fluorite deposit at Bozijan, Markazi Province, Iran. J. Geochem. Explor. https://doi.org/10.1016/j.gexplo.2011. 08.005.

Ehya, F., 2012. Rare earth element and stable isotope (O, S) geochemistry of barite from the Bijgan deposit, Markazi Province. Iran. Min. Petrol. 104, 81–93.

Ehya, F., Lotfi, M., Rasa, I., 2010. Emarat carbonate-hosted Zn–Pb deposit, Markazi Province, Iran: a geological, mineralogical and isotopic (S, Pb) study. J. Asian Earth Sci. 37, 186–194.

Esmaeili Sevieri, A., Karimpour, M.H., Malekzadeh Shafaroudi, A., Mahboubi, A., Song, Y., 2019. Irankuh lead-zinc mining district, southern Isfahan, Iran: Evidences of geology, fluid inclusion and isotope geochemistry. Period. Mineral. 88, 277–296.

Evans, N.J., Byrne, J.P., Keegan, J.T., Dotter, L.E., 2005. Determination of uranium and thorium in zircon, apatite, and fluorite: Application to laser (U-Th)/He thermochronology. J. Anal. Chem. 60, 59–65.

Fanlo, I., Touray, J.C., Subías, I., Fernandez-Nieto, C., 1998. Geochemical patterns of a sheared fluorite vein, Parzan. Spanish Central Pyrenees. Miner. Deposita 33, 620–632.

Faulkner, D.R., Jackson, C.A.L., Lunn, R.J., Schlische, R.W., Shipton, Z.K., Wibberley, C. A.J., Withjack, M.O., 2010. A review of recent developments concerning the structure, mechanics and fluid flow properties of fault zones. J. Struct. Geol. 32, 1557–1575.

Fleet, H.J., Henderson, P., Kepme, D.D.C., 1976. Rare earth element and related chemistry of some drilled Southern Indian Ocean basalts and volcanogenic sediments. J. Geophys. Res. 81, 4257–4268.

Forghani-Tehrani, G., 2003. Genetical and geochemical studies of Komsheche barite deposit, Esfahan province. M.S. thesis. Shiraz University (263 pp in Persian).

Fossen, H., 2010. Structural Geology, first ed. Cambridge University Press, Cambridge, UK. https://doi.org/10.1017/CBO9780511777806.

Francois, T., Agard, P., Bernet, M., Meyer, B., Chung, S.L., Zarrinkoub, M.H., Burov, E., Monie, P., 2014. Cenozoic exhumation of the internal Zagros: First constraints from low-temperature thermochronology and implications for the build-up of the Iranian plateau. Lithos 206-207, 100–112. https://doi.org/10.1016/j.lithos. 2014.07.021.

Freslon, N., Bayon, G., Toucanne, S., Bermell, S., Bollinger, C., Chéron, S., Etoubleau, J., Germain, Y., Khripounoff, A., Ponzevera, E., Rouget, M.L., 2014. Rare earth elements and neodymium isotopes in sedimentary organic matter. Geochim. Cosmochim. Acta 140, 177–198.

Fürsich, F.T., Hautmann, M., Senowbari-Daryan, B., SeyedEmami, K., 2005a. The Upper Triassic Nayband and Darkuh formations of east-central Iran: Stratigraphy, facies patterns and biota of extensional basins on an accreted terrane. Beringeria 35, 53–133.

Fürsich, F.T., Wilmsen, M., Seyed-Emami, K., Cecca, F., Majidifard, M.R., 2005b. The upper Shemshak Formation (Toarcian–Aalenian) of the Eastern Alborz (Iran). Biota and palaeoenvironments during a transgressive–regressive cycle. Facies 51, 365–384.

Fürsich, F.T., Wilmsen, M., Seyed-Emami, K., Majidifard, M.R., 2009. Lithostratigraphy of the Upper Triassic–Middle Jurassic Shemshak Group of Northern Iran. In: Brunet, M.F., Wilmsen, M., Granath, J.W. (Eds.), South Caspian to central Iran Basins. Geol. Soci. London, Special Publications 312, 129–160.

Fürsich, F.T., Pan, Y., Wilmsen, M., Majidifard, M.R., 2016. Biofacies, taphonomy, and paleobiogeography of the Kamar-e-Mehdi Formation of east-central Iran, a Middle to Upper Jurassic shelf lagoon deposit. Facies 62, 1–23. https://doi.org/10.1007/s10347-015-0452-6.

Galindo, C., Tornos, F., Darbyshire, D.P.F., Casquet, C., 1994. The age and origin of the barite-fluorite (Pb-Zn) veins of the Sierra del Guadarrama (Spanish Central System, Spain): a radiogenic (Nd, Sr) and stable isotope study. Chem. Geol. 112, 351–364. https://doi.org/10.1016/0009-2541(94)90034-5.

Genç, Y., 2006. Genesis of the Neogene interstratal karst-type Pöhrenk fluorite-barite (± lead) deposit (Kırşehir, Central Anatolia, Turkey). Ore Geol. Rev. 29, 105–117.

Ghasemi-Nejad, E., Asadi, M., Shahmoradi, M., Aghanabati, A., Mohtat, T., 2013. Palynostratigraphy and reconsideration of the Shemshak Group in north Isfahan (Kashan-Zefreh) based on Dinoflagellate Cysts. Sci. Q. J. Geosci. 86, 99–106 (in Persian with English abstract).

Ghazban, F., McNutt, R.H., Schwarcz, H.P., 1994. Genesis of sediment-hosted Zn-Pb-Ba deposits in the Irankuh district, Esfahan area, west-central Iran. Econ. Geol. 89, 1262–1278.

Ghorbani, M., 2008. Economic geology ore deposits of Iran. Arianzamin Press, Tehran.

Ghorbani, M., 2013. The economic geology of Iran: mineral deposits and natural resources. Springer Science Business Media, Dordrecht. https://doi.org/10.1007/978-94-007-5625-0.

Ghorbani, M., Momenzadeh, M., 1994. Mineralization phases of Iran. In: In: 13th congregation of earth scientists. Iran, Geological Survey of (in Persian).

Goldberg, E.D., Koide, M., Schmitt, R.A., Smith, R.H., 1963. Rare-earth distributions in the marine environment. J. Geophys. Res. 68, 4209–4217.

Gorjizad, H., 1995. Geology, mineralogy, facies analysis and the genesis of Pachi-Miana deposit, East Central Alborz Iran. M.S. thesis. Tarbiat Modares University, Iran (in Persian).

Graaf, S.D., Lüders, V., Banks, D.A., Sośnicka, M., Reijmer, J.J.G., Kaden, H., Vonhof, H. B., 2019. Fluid evolution and ore deposition in the Harz Mountains revisited: isotope and crush-leach analyses of fluid inclusions. Miner. Deposita. https://doi.org/10.1007/s00126-019-00880-w.

Griffith, E.M., Paytan, A., 2012. Barite in the ocean-occurrence, geochemistry and palaeoceanographic applications. Sedimentology 59, 1817–1835.

Guichard, F., Church, T.M., Treuil, M., Jaffrezic, H., 1979. Rare earths in barites: distribution and effects on aqueous partitioning. Geochim. Cosmochim. Acta 43, 983–997.

Gültekin, A.H., Örgün, Y., Suner, F., 2003. Geology, mineralogy and fluid inclusion data of the Kizilcaoren fluorite-barite-REE deposit, Eskisehir. Turkey. J. Asian Earth Sci. 21, 365–376.

Habibi, T., Yazdi, M., Zarepoor, S., Parvanehnejad Shirazi, M., 2013. Late Devonian fish micro-remains from Central Iran. Geopersia 3 (1), 25–34.

Hanilçi, N., Öztürk, H., Kasapçı, C., 2019. Carbonate- hosted Pb-Zn deposits of Turkey. In: Pirajno, F., Unlu, T., Donmez, C., Bahadir Shahin, M. (Eds.), Mineral Resources of Turkey, Solid Earth Science, 16. Springer Nature, Switzerland AG, pp. 497–533.

Hanilçi, N., Öztürk, H., Banks, D., 2020. Geological, geochemical and microthermometric characteristics of the Hakkari region Zn-Pb deposits, SE Turkey. Ore Geol. Rev. 125, 103667.

Hanor, J.S., 2000. Barite-celestine geochemistry and environments of formation. In: Alpers, C.N., Jambor, J.L., Nordstrom, D.K. (Eds.), Reviews in Mineralogy & Geochemistry-Sulfate Minerals 40. Mineralogical Society of America, pp. 193-275.

Hassanzadeh, J., Wernicke, B.P., 2016. The Neotethyan Sanandaj-Sirjan zone of Iran as an arche type for passive margin-arc transitions. Tectonics 35, 586–621. https://doi.org/10.1002/2015TC003926.

Hein, J.R., Zierenberg, R.A., Maynard, J.B., Hannington, M.D., 2007. Multifarious barite-forming environments along a rifted continental margin. Southern California Borderland. Deep-Sea Res. II 54, 1327–1349.

Hosseinkhani, A., Molasalehi, F., 2013. Lead and silver mineralogical studies and lead isotope investigations in Ahangaran mine, Malayer, Iran. Scientific Quarterly Journal Geosciences 24 (94), 359–368 (in Persian with English abstract).

Hu, H., Stern, R.J., 2020. Early Cretaceous subduction initiation beneath southern Tibet caused the northward flight of India. Geosci. Front. https://doi.org/10.1016/j.gsf.2020.01.010.

Jackson, J., 1992. Partitioning of strike-slip and convergent motion between Eurasia and Arabia in eastern Turkey and the Caucasus. J. Geophys. Res. Solid Earth 97, 12471–12479.

Jemmali, N., Souissi, F., Vennemann, T.W., Villa, I.M., 2011. Genesis of the Jurassic carbonate-hosted Pb–Zn deposit of Jebel Ressas (North-Eastern Tunisia): evidence from mineralogy, chemistry, and isotopic composition of sulphides and Triassic rocks. Resour. Geol. 61, 367–383.

Jemmali, N., Carranza, E.J.M., Zemmel, B., 2017. Isotope geochemistry of Mississippi Valley Type stratabound F-Ba-(Pb-Zn) ores of Hammam Zriba (Province of Zaghouan, NE Tunisia). Chem. Erde. 77 (3), 477–486.

Jemmali, N., Rddad, L., Souissi, F., Carranza, E.J.M., 2019. The ore genesis of the Jebel Mecella and Sidi Taya F-Ba (Zn-Pb) Mississippi Valley-type deposits, Fluorite Zaghouan Province, NE Tunisia, in relation to Alpine orogeny: Constraints from geological, sulfur, and lead isotope studies. Comptes rendus-Geoscience 351, 312–320.

Jian, L., Sun, H., Gao, J.G., 2015. Fluorite REE characteristics of the Diyanqinamu Mo deposit, Inner Mongolia. China. Chin. J. Geochem 34, 610–619.

Jiang, S.Y., Wang, R.C., Xu, X.S., Zhao, K.D., 2005. Mobility of high field strength elements (HFSE) in magmatic-, metamorphic-, and submarine-hydrothermal systems. Phys. Chem. Earth 30, 1020–1029.

Johannesson, K.H., Lyons, W.B., 1995. Rare-earth element geochemistry of Colour Lake, an acidic freshwater lake on Axel Heiberg Island, Northwest Territories, Canada. Chem. Geol. 119, 209–223.

Jolivet, L., Faccenna, C., 2000. Mediterranean extension and the Africa-Eurasia collision. Tectonics 19, 1095–1106. https://doi.org/10.1029/2000TC900018.

Jørgensen, B.B., Isaksen, M.F., Jannasch, H.W., 1992. Bacterial sulfate reduction above 100 °C in deep-sea hydrothermal vent sediments. Science 258, 1756–1757.

Kargaranbafghi, F., Foeken, J.P.T., Guest, B., Stuart, F.M., 2012. Cooling history of the Chapedony metamorphic core complex, Central Iran: Implications for the Eurasia-Arabia collision. Tectonophysics 524-525, 100–107. https://doi.org/10.1016/j.tecto.2011.12.022.

Karimpour, M.H., Sadeghi, M., 2018. Dehydration of hot oceanic slab at depth 30–50 km: KEY to formation of Irankuh-Emarat Pb-Zn MVT belt, Central Iran. J. Geochem. Explor. 194, 88–103.

Koepnick, R.B., Denison, R.E., Burke, W.H., Hetherington, E.A., Dahl, D.A., 1990. Construction of the Triassic and Jurassic portion of the Phanerozoic curve of seawater ^{87}Sr/^{86}Sr: Chem. Geol. (Isotope Geoscience Section) 80, 327–349.

Königshof, P., Da Silva, A.C., Suttner, T.J., Kido, E., Waters, J., Carmichael, S.K., Jansen, U., Pas, D., Spassov, S., 2016. Shallow-water facies setting around the Kačák Event: a multidisciplinary approach. Geol. Soci. London. Special Publications 423, 171–199.

Kontak, D.J., Sangster, D.F., 1998. Aqueous and liquid petroleum inclusions in barite from the Walton deposit, Nova Scotia, Canada: A carboniferous, carbonate-hosted Ba-Pb-Zn-Cu-Ag deposit. Econ. Geol. 93, 845–868.

Korte, C., Kozur, H.W., Bruckschen, P., Veizer, J., 2003. Strontium isotope evolution of Late Permian and Triassic seawater. Geochim. Cosmochim. Acta 67, 47–62. https://doi.org/10.1016/S0016-7037(02)01035-9.

Kouhestani, H., Mokhtari, M.A.A., 2017. geology of the ore and study of the fluid inclusion in Jarin barite-fluorite deposit, southeastern Zanjan. J. Advanced Appl. Geol. 25, 1–15 (in Persian).

Kraemer, D., Viehmann, S., Banks, D., Sumoondur, A.D., Koeberl, C., Bau, M., 2019. Regional variations in fluid formation and metal sources in MVT mineralization in the Pennine Orefeld, UK: Implications from rare earth element and yttrium distribution, Sr-Nd isotopes and fluid inclusion compositions of hydrothermal vein fluorites. Ore Geol. Rev. 107, 960–972.

Kyser, T.K., 2007. Fluids, basin analysis, and mineral deposits. Geofluids 7 (2), 238–257.

Lanari, R., Faccenna, C., Fellin, M.G., Essaifi, A., Nahid, A., Medina, F., Youbi, N., 2020. Tectonic evolution of the western High Atlas of Morocco: oblique convergence, reactivation, and transpression. Tectonics 39 (3) p.e2019TC005563.

Leach, D.L., Bradley, D.C., Huston, D., Pisarevsky, S.A., Taylor, R.D., Gardoll, S.J., 2010. Sediment-hosted lead-zinc deposits in Earth history. Econ. Geol. 105, 593–625. https://doi.org/10.2113/gsecongeo.105.3.593.

Lepetit, P., Aehnelt, M., Viereck, L., Strauss, H., Abratis, M., Fritsch, S., Malz, A., Kukowski, N., Totsche, K.U., 2019. Intraformational fluid flow in the Thuringian

Syncline (Germany)-Evidence from stable isotope data in vein mineralization of Upper Permian and Mesozoic sediments. Chem. Geol. 523, 133–153.

Liu, Y.C., Yang, Z., Tian, S., Song, Y.C., Zhang, H.R., 2015. Fluid origin of fluorite-rich carbonate-hosted Pb-Zn mineralization of the Himalayan-Zagros collisional orogenic system: A case study of the Mohailaheng deposit, Tibetan Plateau. China. Ore Geol. Rev. 70, 546–561.

Liu, Y.C., Kendrick, M.A., Hou, Z.Q., Yang, Z.S., Tian, S.H., Song, Y.C, Honda, M., 2017. Hydrothermal fluid origins of carbonate-hosted Pb-Zn deposits of the Sanjiang thrust belt, Tibet: Indications from noble gases and halogens. Econ. Geol. 112, 1247-1268.

Liu, Y.C., Song, Y.C., Fard, M., Zhou, L.M., Hou, Z.Q., Kendrick, M.A., 2019. Pyrite Re-Os age constraints on the Irankuh Zn-Pb deposit, Iran, and regional implications. Ore Geol. Rev. 104, 148–159.

Loges, A., Wagner, T., Barth, M., Bau, M., Göb, S., Markl, G., 2012. Negative Ce anomalies in Mn oxides: the role of Ce^{4+} mobility during water–mineral interaction. Geochim. Cosmochim. Acta 86, 296–317.

Lotfi, M., Hekmatian, M., Shabani, A.A., Mokhtari, M., 2015. Geology and Origin of Oras-Kuh Pb-Zn Deposit in Eastern Alborz (Semnan Province). Sci. Quart. J. Geosci. 24, 73–84.

Lüders, V., Möller, P., 1992. Fluid evolution and ore deposition in the Harz mountains (Germany). Eur. J. Mineral. 4, 1053–1068. https://doi.org/10.1127/ejm/4/5/1053.

Magotra, R., Namga, S., Singh, P., Arora, N., Srivastava, P.K., 2017. A new classification scheme of fluorite deposits. Int. J. Geosci. 8, 599–610. https://doi.org/10.4236/ijg.2017. 84032.

Mannani, M., Yazdi, M., 2009. Late Triassic and Early Cretaceous sedimentary sequences of the northern Isfahan Province (Central Iran): stratigraphy and paleoenvironments. Boletín de la Sociedad Geológica Mexicana 61, 367–374.

Margoum, D., Bouabdellah, M., Klügel, A., Banks, D.A., Castorina, F., Cuney, M., Jébrak, M., Bozkaya, G., 2015. Pangea rifting and onward pre-central Atlantic opening as the main ore-forming processes for the genesis of the Aouli REE-rich fluorite-barite vein system, Upper Moulouya District. Morocco. J. Afr. Earth Sci. 108, 22–39.

Martin, J.M., Høgdahl, O., Philippot, J.C., 1976. Rare earth element supply to the ocean. J. Geophys. Res. 81, 3119–3124.

Mattei, M., Cifelli, F., Muttoni, G., Rashid, H., 2015. Post-Cimmerian (Jurassic–Cenozoic) paleogeography and vertical axis tectonic rotations of Central Iran and the Alborz Mountains. Journal of Asian Earth Sciences 102, 92–101. https://doi.org/10.1016/j.jseaes.2014.09.038.

Maynard, J.B., Okita, P.M., 1991. Bedded barite deposits in the United States, Canada, Germany, and China; two major types based on tectonic setting. Econ. Geol. 86, 364–376.

McArthur, J.M., Howarth, R.J., Bailey, T.R., 2001. Strontium isotope stratigraphy: Lowess Version 3: Best-fit to the marine Sr-isotope curve for 0 to 509 Ma and accompanying look-up table for deriving numerical age. J. Geol. 109, 155–170.

McArthur, J.M., Howarth, R.J., Shields, G.A., 2012. Strontium isotope stratigraphy. The geologic time scale 1, 127–144.

McQuarrie, N., van Hinsbergen, D.J., 2013. Retrodeforming the Arabia-Eurasia collision zone: Age of collision versus magnitude of continental subduction. Geology 41, 315–318.

Mehraban, Z., 2016. Geochemistry of REEs in the fluorite (±Pb, Ba) mine of Savadkuh region, Mazandaran province. M.S. thesis. Golestan University (93 pp in Persian).

Meyer, M., Brockamp, O., Clauer, N., Renk, A., Zuther, M., 2000. Further evidence for a Jurassic mineralizing event in central Europe: K–Ar dating of hydrothermal alteration and fluid inclusion systematics in wall rocks of the Käfersteige fluorite vein deposit in the northern Black Forest. Germany. Miner. Deposita 35 (8), 754–761.

Mirnejad, H., Simonetti, A., Molasalehi, F., 2011. Pb isotopic compositions of some Zn-Pb deposits and occurrences from Urumieh Dokhtar and Sanandaj–Sirjan zones in Iran. Ore Geol. Rev. 39, 181–187. https://doi.org/10.1016/j.oregeorev.2011.02.002.

Moghaddasi, S.J., Tale-Fazel, E., Banifatemi, A.S., 2016. Fluid evolution during mineralization of Atashkuh fluorite-barite (+sulfide) deposit, south of Delijan. J. Econ. Geol. 8, 167–180.

Möller, P., Parekh, P.P., Schneider, H.J., 1976. The application of Tb/Ca–Tb/La abundance ratios to problems of fluorspar genesis. Miner. Deposita 11, 111–116.

Möller, P., Schulz, S., Jacob, K.H., 1980. Formation of fluorite in sedimentary basins. Chem. Geol. 31, 97–117.

Möller, P., Giese, U., Dulski, P., 1994. Behaviour of REE in alteration processes of granites. In: Seltman, R., Kämpf, H., Möller, P. (Eds.), Metallogeny of Collisional Orogens. Czech Geological Survey, Prague, pp. 368–374.

Momenzadeh, M., 1976. Stratabound lead–zinc ores in the lower Cretaceous and Jurassic sediments in the Malayer-Esfahan district (west central Iran), lithology, metal content, zonation and genesis. Heidelberg. Ph.D. thesis. University of Heidelberg (300 pp).

Mondillo, N., Balassone, G., Boni, M., Marino, A., 2017. Evaluation of the amount of rare earth elements -REE in the Silius fluorite vein system (SE Sardinia, Italy). Period. Mineral. 86, 121–132.

Morley, C.K., Kongwung, B., Julapour, A.A., Abdolghafourian, M., Hajian, M., Waples, D., Warren, J., Otterdoom, H., Srisuriyon, K., Kazeni, H., 2009. Structural development of a major late Cenozoic basin and transpressional belt in central Iran: The Central Basin in the Qom-Saveh area. Geosphere 5. https://doi.org/10.1130/GES00223.1, 325-1.

Mouthereau, F., Lacombe, O., Vergés, J., 2012. Building the Zagros collisional orogen: Timing, strain distribution and the dynamics of Arabia/Eurasia plate convergence. Tectonophysics 532-535, 27–60.

Movahednia, M., Rastad, E., Rajabi, A., Maghfouri, S., González, F.J., Alfonso, P., Choulet, F., Canet, C., 2020. The Ab-Bagh Late Jurassic-Early Cretaceous sediment-hosted Zn-Pb deposit, Sanandaj-Sirjan zone of Iran: Ore geology, fluid inclusions and (S–Sr) isotopes. Ore Geol. Rev. 121 https://doi.org/10.1016/j.oregeorev.2020.103484.

Munoz, M., Premo, W.R., Courjault-Radé, P., 2005. Sm–Nd dating of fluorite from the worldclass Montroc fluorite deposit, southern Massif Central. France. Miner. Deposita 39, 970–975.

Nabiloo, F., Shafiei Bafti, B., Amini, A., 2017. Diagenetic and post-diagenetic fabrics in the Kamarposht fluorite mine (east of Mazandaran province): Explanation and genetic interpretation. J. Econ. Geol. 9, 483–507.

Nadoll, P., Rehm, M., Duschl, F., Klemd, R., Kraemer, D., 2018. REY and trace element chemistry of fluorite from post-Variscan hydrothermal veins in Paleozoic units of the north German basin. Geosciences 8 (11). https://doi.org/10.3390/geosciences8080283.

Navabpour, P., Angelier, J., Barrier, E., 2007. Cenozoic post-collisional brittle tectonic history and stress reorientation in the High Zagros Belt (Iran, Fars Province). Tectonophysics 432, 101–131.

Nielsen, H., Ricke, W., 1964. Schwefel-Isotopenverhältnisse von Evaporiten aus Deutschland; Ein Beitrag zur Kenntnis von δ^{34}S im Meerwasser-Sulfat. Geochim. Cosmochim. Acta 28, 577–591.

Niroomand, S., Haghi, A., Rajabi, A., Tabbakh Shabani, A.A., Song, Y.C., 2019. Geology, isotope geochemistry and fluid inclusion investigation on the Robat Zn-Pb-Ba deposit in the Malayer-Esfahan metallogenic belt, Iran. Ore Geol. Rev. 112, 103040.

Nozaki, Y., 2001. Rare earth elements and their isotopes. Encycl. Ocean Sci. 4, 2354–2366.

Nützel, A., Mannani, M., Senowbari-Daryan, B., Yazdi, M., 2010. Gastropods from the Late Triassic Nayband Formation (Iran), their relationships to other Tethyan faunas and remarks on the Triassic gastropod body size problem. Neues Jahrbuch für Geologie und Paläontologie-Abhandlungen 256 (2), 213–228.

Omenetto, P., 1979. Significant ore fabric relationships in the lead, zinc, fluorite and barite deposits of the Triassic province (Italian southern Alps). Annales de la Societe Geologique de Belgique 102, 519–529.

Öztürk, H., Altuncu, S., Hanilçi, N., Kasapçı, C., Goodenough, K.M., 2019. Rare earth element-bearing fluorite deposits of Turkey: an overview. Ore Geol. Rev. 105, 423–444.

Paytan, A., Kastner, M., Martin, E.E., Macdougall, J.D., Herbert, T., 1993. Marine barite as a monitor of seawater strontium isotope composition. Nature 366, 445–449.

Paytan, A., Kastner, M., Campbell, D., Thiemens, M.H., 1998. Sulfur isotope composition of Cenozoic seawater sulfate. Science 282, 1459.

Paytan, A., Mearon, S., Cobb, K., Kastner, M., 2002. Origin of marine barite deposits: Sr and S isotope characterization. Geology 30, 747–750.

Pazhkhzade, L., Ebrahimi Nasrabadi, K., Vatanpour, H.R., Ghaemi, F., Darvishi Khatooni, J., 2018. Mineralization and fluid evolution during mineralization of Sefidkouh fluorite deposit, north west of Torbate Jam. Iran. J. Crystallography and Mineralogy 26, 209–218 (in Persian).

Pearce, J.A., Stern, R.J., 2006. Origin of Back-arc Basin Magmas: Trace Element and Isotope Perspectives.

Pearce, J.A., Harris, N.W., Tindle, A.G., 1984. Trace element discrimination diagrams for the tectonic interpretation of granitic rocks. J. Petrol 25, 956–983.

Petit, J.P., 1987. Criteria for the sense of movement on fault surfaces in brittle rocks. J. Struct. Geol. 9, 597–608. https://doi.org/10.1016/0191-8141(87)90145-3.

Pi, T., Solé, J., Taran, Y., Alfonso, P., 2004. Role of water-rock interaction in the formation of La Azul fluorite deposit, southern Mexico. In: Wanty, Seal, I.I. (Eds.), Water-Rock Interaction 11, vol. 1. Taylor & Francis Group, London, pp. 299–302 (ISBN 905809 6416).

Pi, T., Solé, J., Taran, Y., 2005. (U–Th)/He dating of fluorite: application to the La Azul fluorspar deposit in the Taxco mining district, Mexico. Miner. Deposita 39, 976–982.

Piqué, À., Canals, À., Grandia, F., Banks, D.A., 2008. Mesozoic fluorite veins in NE Spain record regional base metal-rich brine circulation through basin and basement during extensional events. Chem. Geol. 257 (1-2), 139–152.

Pirouzi, M., Ghaderi, N., Rashinejad-Omran, N., Rastad, E., 2009. New evidences on mineralization, diagenesis and fluid inclusions at Kamar-Mehdi stratabound fluorite deposit, southwest Tabas. Iran. J. Crystallography and Mineralogy 17, 83–94 (in Persian).

Qishlaqi, A., Moore, F., 2006. Recognition of Pinavand fluorite mines occurrence based on geothermometry and REE data. Iran. J. Crystalography and Mineralogy 2, 325–338 (in Persian).

Radfar, J., Amini Jehragh, M.R., Emami, M.H., 1999. Geological map of Ardestan, scale 1:100000. Geological Survey of Iran, Tehran, Iran.

Rahimpour-Bonab, H., Shekarifard, A., 2002. Barite ore deposits in the Central Iran-Ardakan province: Genesis and Alterations. Iran. Int. J. Sci. 3, 69–91.

Rajabi, A., Rastad, E., Canet, C., 2012. Metallogeny of Cretaceous carbonate-hosted Zn-Pb deposits of Iran: geotectonic setting and data integration for future mineral exploration. Int. Geol. Rev. 54, 1649–1672.

Rajabi, A., Rastad, E., Canet, C., 2013. Metallogeny of Permian–Triassic carbonate-hosted Zn–Pb and F deposits of Iran: A review for future mineral exploration. Australian Journal of Earth Sciences. An International Geoscience Journal of the Geological Society of Australia 60, 197–216.

Rajabi, A., Mahmoodi, P., Rastad, E., Niroomand, S., Canet, C., Alfonso, P., Tabbakh Shabani, A.A., Yarmohammadi, A., 2019. Comments on "Dehydration of hot oceanic slab at depth 30–50 km: Key to formation of Irankuh-Emarat Pb-Zn MVT belt, Central Iran" by Mohammad Hassan Karimpour and Martiya Sadeghi. J. Geochem. Explor. 205, 106346.

Rajabzadeh, M.A., 2007. A fluid inclusion study of a large MVT barite-fluorite deposit: Komshecheh, Central Iran. Iran. J. Sci. Technology 31, 73–87.

Ramboz, C., Charef, A., 1988. Temperature, pressure, burial history, and paleohydrogeology of the Les Malines Pb-Zn deposit: reconstruction from aqueous inclusions in barite. Econ. Geol. 83, 784–800.

Rastad, E., 1981. Geological, mineralogical and ore facies investigations on the Lower Cretaceous stratabound Zn-Pb-Ba-Cu deposits of the Irankuh mountain range, Isfahan, west central Iran. Germany. Ph.D. thesis. Heidelberg University (334 pp).

Reesman, R.H., 1968. Rb-Sr analyses of some sulfide mineralization. Earth Planet. Sci. Lett. 5, 23–26.

Reuter, M., Piller, W.E., Harzhauser, M., Mandic, O., Berning, B., Rögl, F., Hamedani, A., 2007. The Oligo-Miocene Qom Formation (Iran): Evidence for an early Burdigalian restriction of the Tethyan Seaway and closure of its Iranian gateways. Int. J. Earth Sci. 98, 627–650.

Rezaei-Azizi, M., Abedini, A., Alipour, S., Bagheri, S., 2018. The Laal-Kan fluorite deposit, Zanjan Province, NW Iran: constraints on REE geochemistry and fluid inclusions. Arabian Journal of Geosciences 11, 719–815. https://doi.org/10.1007/s12517-018-4055-8.

Richards, J., Sholeh, A., 2016. The Tethyan tectonic history and Cu-Au metallogeny of Iran. Special Publication 19, 193–212.

Rossetti, F., Aldega, L., Tecce, F., Balsamo, F., Billi, A., Brilli, M., 2011. Fluid flow within the damage zone of the Boccheggiano extensional fault (Larderello–Travale geothermal field, central Italy): structures, alteration and implications for hydrothermal mineralization in extensional settings. Geol. Mag. 148, 558–579.

Rostami, G., 2001. Facies analysis, Geochemistry and genesis of F (Zn-Pb-Ba) Milakuh-Touyeh deposit in Soltanieh Formation (Soutwest Damghan). M.S. thesis. Tarbiat Modares University (in Persian).

Rudnick, R.L., Gao, S., 2003. Composition of the continental crust. Crust 3, 1–64.

Safaei, H., Taheri, A., Vaziri-Moghaddam, H., 2008. Structural analysis and evolution of the Kashan (Qom-Zefreh) Fault, Central Iran. J. Appl. Sci. 8, 1426–1434.

Salehi, M.A., Tadayon, M., 2020. Early Cretaceous sedimentary provenance and structural evolution of the central Sanandaj–Sirjan Zone, Iran: implications for palaeogeographic reconstructions of the northern Neo-Tethyan margin. Int. Geol. Rev. 62 (11), 1359–1386.

Salehi, M.A., Mazroei Sebdani, Z., Pakzad, H.R., Bahrami, A., Fürsich, F.T., Heubeck, C., 2018. Provenance and palaeogeography of uppermost Triassic and Lower Cretaceous terrigenous rocks of central Iran. In: Reflection of the Cimmerian events: Neues Jahrbuch für Geologie und Paläontologie- Abhandlungen, 288, pp. 49–77. https://doi.org/10.1127/njgpa/2018/0723.

Sallet, R., Moritz, R., Fontignie, D., 2005. The use of vein fluorite as probe for paleofluid REE and Sr–Nd isotope geochemistry: the Santa Catarina Fluorite District, Southern Brazil. Chem. Geol. 223, 227–248.

Salvini, F., Billi, A., Wise, D.U., 1999. Strike-slip fault-propagation cleavage in carbonate rocks: The Mattinata Fault Zone, Southern Apennines, Italy. J. Struct. Geol. 21, 1731–1749. https://doi:10.1016/S0191-8141(99)00120-0.

Sánchez, V., Corbella, M., Fuenlabrada, J.M., Vindel, E., Martín-Crespo, T., 2006. Sr and Nd isotope data from the fluorspar district of Asturias, northern Spain. Journal of Geochemical Exploration 89 (1–3), 348–350.

Sánchez, V., Vindel, E., Martin-Crespo, T., Corbella, M., Cardellach, E., Banks, D., 2009. Sources and composition of fluids associated with fluorite deposits of Asturias (N Spain). Geofluids 9, 338–355.

Sánchez, V., Cardellach, E., Corbella, M., Vindel, E., Martin-Crespo, T., Boyce, A.J., 2010. Variability in fluid sources in the fluorite deposits from Asturias (north Spain): further evidences from REE, radiogenic (Sr, Sm, Nd) and stable (S, C, O) isotope data. Ore Geol. Rev. 37, 87–100.

Sarjoughian, F., Kananian, A., 2017. Zircon U-Pb geochronology and emplacement history of intrusive rocks in the Ardestan section, central Iran. Geol. Acta 15, 25–36.

Sarjoughian, F., Lentz, D., Kananian, A., Ao, S., Xiao, W., 2017. Geochemical and isotopic constraints on the role of juvenile crust and magma mixing in the UDMA magmatism, Iran: evidence from mafic microgranular enclaves and cogenetic granitoids in the Zafarghand igneous complex. Int. J. Earth Sci. 107, 1127–1151.

Scheffer, C., Tarantola, A., Vanderhaeghe, O., Voudouris, P., Spry, P.G., Rigaudier, T., Photiades, A., 2019. The Lavrion Pb-Zn-Ag–rich vein and breccia detachment-related deposits (Greece): Involvement of evaporated seawater and meteoric fluids during postorogenic exhumation. Econ. Geol. 114, 1415–1442.

Scher, H.D., Griffith, E.M., Buckley Jr., W.B., 2014. Accuracy and precision of ^{88}Sr/^{86}Sr and ^{87}Sr/^{86}Sr measurements by MC-ICPMS compromised by high barium concentrations. Geochemistry, Geophysics, Geosystems 15, 499–508. https://doi.org/10.1002/2013GC005134.

Schneider, J., Boni, M., Lapponi, F., Bechstädt, T., 2002. Carbonate-hosted zinc-lead deposits in the Lower Cambrian of Hunan, South China: a radiogenic (Pb, Sr) isotope study. Econ. Geol. 97 (8), 1815–1827.

Schönenberger, J., Köhler, J., Markl, G., 2008. REE systematics of fluorides, calcite and siderite in peralkaline plutonic rocks from the Gardar Province, South Greenland. Chem. Geol. 247, 16–35.

Schwinn, G., Markl, G., 2005. REE systematic in hydrothermal fluorite. Chem. Geol. 216, 225–248.

Schwinn, G., Wagner, T., Baatartsogt, B., Markl, G., 2006. Quantification of mixing processes in ore-forming hydrothermal systems by combination of stable isotope and fluid inclusion analyses. Geochim. Cosmochim. Acta 70, 965–982.

Senowbari-daryan, B., Rashidi, K., Torabi, H., 2010. Foraminifera and their associations of a possibly Rhaetian section of the Nayband Formation in central Iran, northeast of Esfahan. Facies 56, 567–596.

Shafaezadeh, E., 2012. Mineralogical and fluid inclusion studies of fluorite and barites in the Pinavand area (northeast of Isfahan). M.S. Thesis. University of Isfahan (110 pp in Persian).

Shafaii Moghadam, H., Stern, R.J., 2015. Ophiolites of Iran: Keys to understanding the tectonic evolution of SW Asia: (II) Mesozoic ophiolites. J. Asian Earth Sci. 100, 31–59. https://doi.org/10.1016/j.jseaes.2014. 12.016.

Shafaii Moghadam, H., Whitechurch, H., Rahgoshay, M., Monsef, I., 2009. Significance of Nain-Baft ophiolitic belt (Iran): Short-lived, transtensional Cretaceous back-arc oceanic basins over the Tethyan subduction zone. C. R. Geosci. 341, 1016–1028. https://doi.org/10.1016/j.crte.2009.06.011.

Shamsipour Dehkordi, R., Kermani, N., Bagheri, H., 2011. Geothermometric and isotopic studies of Kohroyeh Pb ore deposit (SW Shahreza). Petrology 1, 35–44 (in Persian).

Sheikholeslami, M.R., 2016. Tectono-stratigraphic evidence for the opening and closure of the Neotethys Ocean in the southern Sanandaj-Sirjan zone, Iran, in Sorkhabi, R. (Eds.), Tectonic evolution, collision, and seismicity of southwest Asia, in honour Manuel Berberian's forty-five years of research contributions. In: Geological Society of America, Boulder, Colorado, SPE525–09, pp. 319–342.

Sibson, R.H., Moore, J.M., Rankin, A.H., 1975. Seismic pumping-a hydrothermal fluid transport mechanism. J. Geol. Soc. London 131, 653–659.

Song, Y.C., Yang, T.N., Zhang, H.R., Liu, Y.C., Hao, H.D., Li, Z., 2015. The Chaqupacha Mississippi Valley-type Pb-Zn deposit, central Tibet: Ore formation in a fold and thrust belt of the India-Asia continental collision zone. Ore Geol. Rev. 70, 533–545.

Sośnicka, M., Lüders, V., 2019. Super-deep, TSR-controlled Phanerozoic MVT type Zn-Pb deposits hosted by Zechstein-2 gas reservoir carbonate (Ca2), Lower Saxony Basin, Germany. Chem. Geol. 508, 62–77.

Souissi, F., Dandurand, J.L., Fortuné, J.P., 1997. Thermal and chemical evolution of fluids during fluorite deposition in the Zaghouan province, north-eastern Tunisia. Miner. Deposita 32, 257–270.

Souissi, F., Jemmali, N., Souissi, R., Dandurand, J.L., 2013. REE and isotope (Sr, S, and Pb) geochemistry to constrain the genesis and timing of the F-(Ba-Pb-Zn) ores of the Zaghouan District (NE Tunisia). Ore Geol. Rev. 55, 1–12.

Stacey, J.S., Kramers, J.D., 1975. Approximation of terrestrial lead isotope evolution by a two-stage model. Earth Planet. Sci. Lett. 26, 207–221.

Stampfli, G.M., Borel, G.D., 2002. A plate tectonic model for the Paleozoic and Mesozoic constrained by dynamic plate boundaries and restored synthetic oceanic isochrons. Earth Planet. Sc. Lett. 196, 17–33. https://doi.org/10.1016/S0012-821X(01)00588-X.

Staude, S., Bons, P.D., Markl, G., 2009. Hydrothermal vein formation by extension-driven dewatering of the middle crust: an example from SW Germany. Earth Planet. Sci. Lett. 286, 387–395.

Staude, S., Göb, S., Pfaff, K., Ströbele, F., Premo, W.R., Mark, G., 2011. Deciphering fluid sources of hydrothermal systems: a combined Sr- and S-isotope study on barite (Schwarzwald, SW Germany). Chem. Geol. 286, 1–20.

Stöcklin, J., 1968. Structural history and tectonics of Iran: a review. aapg bulletin 52, 1229–1258.

Stöcklin, J., 1974. Possible ancient continental margins in Iran. In: Burke, C.A., Drake, C. L. (Eds.), The Geology of Continental Margins. Springer, New York, pp. 873–887.

Subías, I., Fanlo, I., Mateo, E., Billström, K., Recio, C., 2010. Isotopic studies of Pb–Zn–(Ag) and barite Alpine vein deposits in the Iberian Range (NE Spain). Geochemistry 70 (2), 149–158.

Sverjensky, D.A., 1984. Europium redox equilibria in aqueous solution. Earth Planet. Sci. Lett. 67, 70–78.

Symons, D.T.A., Kawaski, K., Tornos, F., Velasco, F., Rosales, I., 2017. Temporal constraints on genesis of the Caravia-Berbes fluorite deposits of Asturias, Spain, from paleomagnetism. Ore Geol. Rev. 80, 754–766.

Tabaei, M., Mehdizadeh, R., Esmaeili, M., 2016. Stratigraphical evidences of the Qom–Zefreh Fault system activity, Central Iran. Journal of Tethys 4, 18–26.

Tadayon, M., 2013. Structure of basin bounded faults in Shahreza area (south of Isfahan) (Central Sanandaj-Sirjan). M.S. thesis. Tarbiat Modares University (96 pp in Persian).

Tadayon, M., Rossetti, F., Zattin, M., Nozaem, R., Calzolari, G., Madanipour, S., Salvini, F., 2017. The Post-Eocene evolution of the Doruneh Fault Region (Central Iran): The intraplate response to the reorganization of the Arabia-Eurasia Collision Zone. Tectonics 36, 3038–3064.

Tadayon, M., Rossetti, F., Zattin, M., Calzolari, G., Nozaem, R., Salvini, F., Faccenna, C., Khodabakhshi, P., 2019. The long-term evolution of the Doruneh Fault region (Central Iran): A key to understanding the spatio-temporal tectonic evolution in the hinterland of the Zagros convergence zone. Geological Journal. https://doi.org/10.1002/gj.3241.

Taghipour, B., Moore, F., Mackizadeh, M.A., 2010. Stable isotope evidences of jarosite–barite mineralization in the Rangan rhyolitic dome NE Isfahan, Iran. Chem. Erde. 70, 377–384.

Talaie, B., Abedini, A., 2012. Investigation of geochemistry and genesis of Qahr-abad fluorite deposit, southeast of Saqqez, Kordestan province. Iran. J. Econ. Geol. 1, 155–168.

Talebian, M., Jackson, J., 2002. Offset on the Main Recent Fault of NW Iran and implications for the late Cenozoic tectonics of the Arabia–Eurasia collision zone. Geophys. J. Int. 150, 422–439.

Tian, S.H., Yang, Z.S., Hou, Z.Q., Liu, Y.C., Gao, Y.G., Wang, Z.L., Song, Y.C., Xue, W.W., Lu, H.F., Wang, F.C., Su, A.N., Li, Z.Z., Wang, Y.X., Zhang, Y.B., Zhu, T., Yu, C.J., Yu, Y.S., 2009. Rb-Sr and Sm-Nd isochron ages of Dongmozhazhua and Mohailaheng Pb-Zn ore deposits in Yushu area, southern Qinghai and their geological implications. Mineral Deposits 28, 747–758 (in Chinese with English abstract).

Tian, S.H., Gong, Y.L., Yang, Z.S., Hou, Z.Q., Liu, Y.C., Song, Y.C., Xue, W.W., Lu, H.F., Wang, F.C., Zhang, Y.B., 2014. Rb-Sr and Sm-Nd isochron ages of the Dongmozhazhua and Mohailaheng Pb-Zn ore deposits in the Yushu area, southern Qinghai and their geological implications. Acta Geologica Sinica-English Edition 88, 558–569.

Tornos, F., Delgado, A., Casquet, C., Galindo, C., 2000. 300 Million years of episodic hydrothermal activity: stable isotope evidence from hydrothermal rocks of the Eastern Iberian Central System. Miner. Deposita 35, 551–569. https://doi.org/10.1007/s001260050261.

Trinkler, M., Monecke, T., Thomas, R., 2005. Constraints on the genesis of yellow fluorite in hydrothermal barite-fluorite veins of the Erzgebirge, Eastern Germany: evidence from optical absorption spectroscopy, rare-element data, and fluid-inclusion investigations. The Canadian Mineralogists 43, 883–898.

Tropper, P., Manning, C.E., 2007. The solubility of fluorite in H_2O and H_2O–NaCl at high pressure and temperature. Chem. Geol. 242 (3–4), 299–306.

Ufrecht, W., Hölzl, S., 2006. Salinare Mineral- und Thermalwässer im Oberen Muschelkalk (Trias) im Großraum Stuttgart-Rückschlüsse auf Herkunft und Entstehung mit Hilfe der ^{87}Sr/^{86}Sr-Strontium-Isotopie. Zeitschrift der deutschen Gesellschaft für Geowissenschaften 157, 299–316.

Uras, Y., Oner, F., Yaman, S., 2003. Geochemistry of fluorite occurrence from Feke (Adana-Turkey) in the East Taurid Mountains. Chem. Erde 63, 55–62.

Vahab-zadeh, G., Khakzad, A., Rasae, I., Mousavi, M.R., 2008. The study of sulfur isotopes of galena and barite in fluorite ore deposits of Savad Koh region. Journal of Sciences (Islamic Azad University) 18, 99–108.

Valentino, G.M., Stanzione, D., 2003. Source processes of the thermal waters from the Phlegraean Fields (Naples, Italy) by means of the study of selected minor and trace elements distribution. Chem. Geol. 194 (4), 245–274.

Valenza, K., Moritz, R., Mouttaqi, A., Fontignie, D., Sharp, Z., 2000. Vein and karst barite deposits in the western Jebilet of Morocco: Fluid inclusion and isotope (S, O, Sr) evidence for regional fluid mixing related to central Atlantic rifting. Econ. Geol. 95, 587–606.

Verdel, C., Wernicke, B.P., Hassanzadeh, J., Guest, B., 2011. A Paleogene extensional arc flare-up in Iran. Tectonics 30, TC3008. https://doi.org/10.1029/2010TC002809.

Walter, B.F., Gerdes, A., Kleinhanns, I.C., Dunkl, I., von Eynatten, H., Kreissl, S., Markl, G., 2018. The connection between hydrothermal fluids, mineralization, tectonics and magmatism in a continental rift setting: Fluorite Sm-Nd and hematite and carbonates U-Pb geochronology from the Rhinegraben in SW Germany. Geochim. Cosmochim. Acta 240, 11–42.

Walter, B.F., Kortenbruck, P., Scharrer, M., Zeitvogel, C., Wälle, M., Mertz-Kraus, R., Markl, G., 2019. Chemical evolution of ore-forming brines–Basement leaching, metal provenance, and the redox link between barren and ore-bearing hydrothermal veins. A case study from the Schwarzwald mining district in SW Germany. Chem. Geol. 506, 126–148.

Wang, G.Z., Liu, S.G., Chen, C.H., 2013. The genetic relationship between MVT Pb-Zn deposits and paleo-oil/gas reservoirs at Heba, southeastern Sichuan basin. Earth Science Frontiers 20, 107–116 (in Chinese).

Whitney, D., Evans, B., 2010. Abbreviations for names of rock-forming minerals. Am. Mineral. 95, 185–187.

Williams-Jones, A.E., Samson, I.M., Olivo, G.R., 2000. The genesis of hydrothermal fluorite-REE deposits in the Gallinas Mountains, New Mexico. Econ. Geol. 95, 327–342.

Wilmsen, M., Fürsich, F.T., Seyed-Emami, K., Majidifard, M.R., 2009. An overview of the stratigraphy and facies development of the Jurassic System on the Tabas Block, East Central Iran. In: Brunet, M.F., Wilmsen, M., Granath, J.W. (Eds.), South Caspian to central Iran Basins, Geological Society of London Special Publications, 312, pp. 323–343.

Wilmsen, M., Fürsich, F., Seyed-Emami, K., Majidifard, M., Zamani-Pedram, M., 2010. Facies analysis of a large-scale Jurassic shelf-lagoon: The Kamar-e-Mehdi Formation of east-central Iran. Facies 56, 59–87. https://doi.org/10.1007/s10347-009-0190-8.

Wilmsen, M., Fürsich, F.T., Majidifard, M.R., 2013. The Shah Kuh Formation, a latest Barremian-Early Aptian carbonate platform of Central Iran (Khur area, Yazd Block). Cretaceous Research 39, 183–194. https://doi.org/10.1016/j.cretres.2012.02.013.

Wilmsen, M., Fürsich, F.T., Majidifard, M.R., 2015. An overview of the Cretaceous stratigraphy and facies development of the Yazd Block, western Central Iran. Journal of Asian Earth Sciences 102, 73–91.

Wiprut, D., Zoback, M.D., 2000. Fault reactivation and fluid flow along a previously dormant normal fault in the northern North Sea. Geology 28 (7), 595–598.

Wolff, R., Dunkl, I., Kempe, U., Eynatten, H.V., 2015. The Age of the latest thermal overprint of tin and polymetallic deposits in the Erzgebirge, Germany: Constraints from fluorite (U-Th-Sm)/He thermochronology. Econ. Geol. 110, 2025–2040.

Wolff, R., Dunkl, I., Kempe, U., Stockli, D., Wiedenbeck, M., Eynatten, H.V., 2016. Variable helium diffusion characteristics in fluorite. Geochim. Cosmochim. Acta 188, 21–34.

Wright, T.J., Ayele, A., Ferguson, D., Kidane, T., Vye-Brown, C., 2016. Magmatic rifting and active volcanism: introduction. Geol. Soc. London Special Publications 420, 1–9.

Zabihitabar, S., Shafiei-Bafti, B., 2015. Mineralogy and occurrence of sulfides, sulfates, and carbonated in the fluorite deposits of eastern Mazandaran province. Iran. J. Geol. 9, 63–77.

Zabihitabar, S., Shafiei, B., Mirnejad, H., 2017. Tracing of sulfur origin from sulfide and sulfate minerals in the fluorite mines of Elika Formation (east of Mazandaran): applications of stable isotope. Iran. J. Geol. 9, 75–92.

Zahedi, M., 1976. geological map of Esfahan, scale 1:250 000, Geological Survey of Iran, Tehran no. 6354.

Zarasvandi, A., Zaheri, N., Pourkaseb, H., Chrachi, A., Bagheri, H., 2014. Geochemistry and fluid-inclusion microthermometry of the Farsesh barite deposit, Iran. Geologos 20 (3), 201–214.

Zartman, R.E., Doe, B.R., 1981. Plumbotectonics-the model. Tectonophysics 75, 135–162.

Zou, H., Zhang, S.T., Chen, A.G., Zeng, Z, 2015. Hydrothermal fluid sources of the Fengjia barite-fluorite deposit in southeast Sichuan, China: Evidence from fluid inclusions and hydrogen and oxygen isotopes. Resour. Geol. 66, 24–36. https://doi. https://doi.org/10.1111/rge.12084.

Zou, H., Fang, Y., Zhang, ST, Zhang, Q., 2017. The source of Fengjia and Langxi barite–fluorite deposits in southeastern Sichuan, China: evidence from rare earth elements and S, Sr, and Sm–Nd isotopic data. Geol. J. 52 (3), 470–488. https://doi. https://doi.org/10.1002/gj.2779.